Feasibility Study for Measuring the $B^- \to D^{(*)0}\eta\ell^-\bar{\nu}$ Branching Fraction

by

Sahar Gholipourverki
B.Sc., University of Tehran, 2017

A Thesis Submitted in Partial Fulfillment of the
Requirements for the Degree of

MASTER OF SCIENCE

in the Department of Physics and Astronomy

Feasibility Study for Measuring the $B^- \to D^{(*)0}\eta\ell^-\bar{\nu}$ Branching Fraction

by

Sahar Gholipourverki
B.Sc., University of Tehran, 2017

Supervisory Committee

Dr. Robert Kowalewski, Supervisor
(Department of Physics and Astronomy)

Dr. J. Michael Roney, Departmental Member
(Department of Physics and Astronomy)

Abstract

Semileptonic B meson decays provide a direct method to measure the parameters of the Cabibbo-Kobayashi-Maskawa (CKM) matrix, which is essential for understanding quark mixing and CP violation in the Standard Model. This thesis presents an exploratory study on the Branching Fraction of the B meson decay mode $B^- \to D^{(*)0}\eta\ell^-\bar{\nu}_\ell$ which has never been measured. Here, ℓ represents either an electron or a muon, ν_ℓ denotes the corresponding lepton neutrino, $D^{(*)}$ refers to either a D meson or its excited state D^*, and η symbolizes the eta meson. In this analysis to reduce the significantly higher occurrence of background events compared to signal candidates, both B mesons are reconstructed semileptonically. The tag-side B meson predominantly decays via $B^+ \to \bar{D}^{(*)0}\ell^+\nu_\ell$. This investigation aims to contribute to a more comprehensive understanding of B meson semileptonic decays by attempting to bridge the gap between the measurements of exclusive semileptonic decay modes and the summation of all measured exclusive semileptonic decays, and improve the understanding of the background in lepton flavor-violating decay modes such as $B \to D^{(*)}\tau\nu_\tau$. This work shows that with 470.78 fb^{-1}, with the MC $BF(B^- \to D^0\eta\ell^-\bar{\nu_\ell}) + BF(B^- \to D^{*0}\eta\ell^-\bar{\nu_\ell}) = 0.008$ where ℓ can be either an electron or a muon, Belle II may be able to measure sum of the branching fraction for the decay of $B^- \to D^0\eta\ell^-\bar{\nu}$ and $B^- \to D^{*0}\eta\ell^-\bar{\nu}$ with more than 5σ significance.

Table of Contents

List of Tables

List of Figures

Acknowledgements

This journey, which began with my departure from Iran, transformed into an adventure of academia and self-discovery, all thanks to the people who journeyed alongside me:

First and foremost, I extend my heartfelt gratitude to my supervisor, **Prof. Robert Kowalewski**, whose guidance was pivotal. He was a mentor who meticulously navigated the intricacies of my analysis from inception to completion and eased the transition to a life thousands of miles away from my family. I have lost count of how many times I reached out with my student-level questions, but he always responded promptly with patience and understanding. Thank you for your unwavering support and your belief in me every step of the way.

I deeply appreciate my co-supervisor, **Prof. Michael Roney**, with his exceptional advice and the discipline of weekly meetings, which greatly improved my presentation skills and confidence. Thank you for your significant impact on my development.

I would also like to sincerely thank my examiner, **Prof. Manuel Franco Sevilla** for his invaluable feedback and kindness during my defense. His approach enhanced my understanding and provided a supportive environment that eased my presentation.

I convey deep appreciation to **Prof. Heather Russell** for her invaluable guidance and insights throughout my project. Her teachings in the Standard Model of Physics profoundly shaped my academic path.

Additionally, I express gratitude to the **staff of the Physics and Astronomy Department**, who were consistently available, friendly, and open, providing essential support.

This thesis reflects not only my efforts but also the steadfast mentorship of my fellow grad friends, **Alex Beaubien, Caleb Miller, Maheyer Shroff, Alberto Nava, Sahar Taghayor, Negar Seif** and **Charlie Chen**. You witnessed how my challenges dissolved into moments of joy, and our fourth-floor gatherings consistently revived my spirits during exhausting days. Your support and camaraderie have been invaluable in helping me navigate through the toughest times.

Dedication

To my brother, **Sadra Gholipourverki**, for taking care of our parents and ensuring they never feel my absence.

To my dad, **Saeid Gholipourverki**, for all his support and for believing in me always.

To my mom, **Nadia Bagheri**, for giving me endless love, teaching me how to cherish others, and showing me how to remain strong in life's storm.

CHAPTER 1

Introduction

Particle physics is the field that looks at the smallest known building blocks of the universe and the forces that govern them. Elementary particles which are the foundation of the Standard Model are divided into three groups. Quarks are the first group of fermions including three types (or flavors). Leptons are the second group of fermions also consisting of three types (or flavors). Bosons or the mediators of the interactions are responsible for carrying the forces. In the Standard Model of particle physics, three of the four fundamental forces – electromagnetism, weak nuclear force, and strong nuclear force – are described along with their respective mediating particles: photons, W and Z bosons, and gluons[1].

The study of B mesons is an important tool for verifying the properties of the Standard Model. B mesons are composed of a bottom antiquark and a second quark that defines its charge mode, such as up (B^+), down (B^0), strange (B_s^0), or charm (B_c^+) [1]. B mesons are particularly important for studying Charge-Parity (CP) violation — a phenomenon where matter and antimatter behave differently [2]. Depending on the final state particles, the B meson can decay hadronically, leptonically, or semileptonically. This analysis will focus on the semileptonic decay mode which offers opportunities for testing the Standard Model. The well-measured semileptonic B decays to $D^{(*)}\ell\nu$, $D^{(*)}\pi\ell\nu$ do not cover all decays to charmed hadronic states $X_c\ell\nu$, leaving unmeasured decays that introduce uncertainties in background predictions for other analyses. Although the semileptonic decays of B mesons to $D^{(*)}\ell\nu$ and $D^{(*)}\pi\ell\nu$ are well measured, they do not cover all possible decays to charmed hadronic states ($B \to X_c\ell\nu$). The absence of measurements for these decay channels introduces uncertainties in the background estimates used in various analyses. Measurement of not-yet-measured B meson decays (e.g. $B^- \to D^{(*)0}\eta\ell^-\bar{\nu}$[1]) stands out because it helps bridge the gap between exclusive and inclusive studies of semileptonic B meson decays [3]

The Belle II experiment, which plays a leading role in particle physics research, operates at the SuperKEKB e^+e^- collider in Tsukuba, Japan. As the successor to the Belle experiment,

[1] We assume charge conjugation invariance.

it is designed to push the boundaries of scientific theories in the Standard Model. A specific focus is on understanding phenomena such as CP violation and the behavior of B mesons [4]. Belle II aims to collect data corresponding to an integrated luminosity of 50 ab^{-1} by the end of its lifetime, representing an approximate 50 times increase compared to the Belle experiment [5]. As a result, it enables researchers to investigate previously inaccessible areas of particle physics, e.g., exploring not-measured decay processes and potential new physics beyond the current theoretical framework [6].

The focus of this thesis is an exploratory study on the measurement of the branching fraction of the signal mode $B^- \to D^{(*)0}\eta\ell^-\bar{\nu}$, where the other B meson goes to $\bar{D}^{(*)0}\ell^+\nu$ in a semileptonic B meson decay. Using simulated MC datasets, the process starts with event selection, reconstruction techniques, and statistical analysis to isolate the signal from background processes. The remaining chapters in this thesis are organized as follows.

Chapter 2 provides an overview of the Standard Model of particle physics, outlining the theoretical framework and its implications. Additionally, it delves into the motivation for measuring the branching fraction of $B^- \to D^{(*)0}\eta\ell^-\bar{\nu}$, highlighting its significance in the understanding of semileptonic B meson decays.

Chapter 3 details the setup of the Belle II detector and its various subdetectors, describing their design and functionality.

Chapter 4 discusses the event selection criteria and the signal and background separation methodologies.

Chapter 5 presents the overview of the signal mode branching fraction study and signal efficiency for the $B^- \to D^{(*)0}\eta\ell^-\bar{\nu}$ decay mode.

Chapter 6 delves into a validation study of the signal efficiency and the branching fraction for $B^- \to D^{(*)0}\eta\ell^-\bar{\nu}$ decay mode. This investigation assesses the initial findings and identifies potential discrepancies or challenges in the measurement process.

Chapter 7 evaluates the selection of double semileptonic decays of charged B mesons, chosen for their comparatively cleaner sample. This thesis is a preliminary feasibility study and is ready for tests with real data in addition to extending the analysis to neutral B mesons.

CHAPTER 2

Standard Model of Particle Physics

This chapter will explore the Standard Model (SM) of particle physics, which explains the smallest parts of matter and the forces that act on them. It starts with a look at elementary particles, and how they interact with each other. A key part of the discussion will focus on B meson decays, how these composite particles contribute to a deeper understanding of the CKM matrix elements and assist in the clarification of CP violation. This exploration aims to provide a clear understanding of these subatomic particles and their significant roles in the world of physics.

2.1 Standard Model Concept

Particle physics, a fundamental branch of physics, delves into the understanding of the smallest known constituents of matter (quarks and leptons) and the interactions (bosons) governing them. Central to particle physics is the Standard Model, a well-established theoretical framework that successfully describes three of the four known fundamental forces – electromagnetic, weak, and strong interactions – and classifies all known elementary particles. Although it provides accurate predictions, the Standard Model is not complete, as it does not include gravity and leaves questions like the nature of dark matter and the imbalance of matter and antimatter in the universe unanswered. Thus, particle physics not only offers a window into the foundational laws that control the microscopic world but also drives the search for new theories and discoveries that extend beyond the current model.

In the Standard Model of particle physics, we categorize the elementary components of the universe into two main groups: fermions and bosons as shown in Figure 2.1.

2.1.1 Fermions

Fermions are a central category of particles in the Standard Model of particle physics, distinctively characterized by their half-integer spin. This unique property, described as spin,

is a basic aspect that influences how fermions behave and interact with each other and with other particles. One of the most crucial principles governing fermions is the Pauli Exclusion Principle, which states that no two identical fermions can occupy the same quantum state at the same time. This principle is essential for understanding the structure of atoms and the vast array of chemical elements in the universe. In addition to their role in forming matter, fermions are also subject to the fundamental forces of nature, such as the strong, weak, and electromagnetic forces, which dictate their interactions at the microscopic level. Their behavior under these forces and their adherence to the Pauli Exclusion Principle are key to the stability and diversity of matter as we know it. Fermions include particles like quarks and leptons:

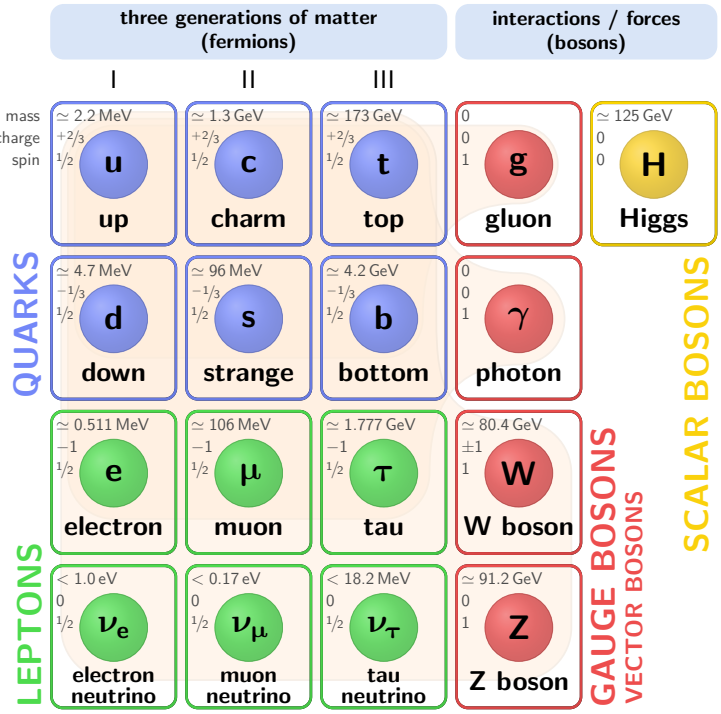

Figure 2.1: **Overview of the Standard Model of Elementary Particles** - This figure displays the fundamental particles within the Standard Model, organized into fermions (quarks and leptons) and bosons (force carriers). Each particle is labeled with its mass, electric charge, and spin, showcasing the diversity and order within the subatomic world. It also shows which bosons mediate interactions among specific sets of particles, in addition to the Higgs boson responsible for mass [7].

- **Quarks**: These half-spin elementary particles come in six types, known as flavors: up, down, charm, strange, top, and bottom. They possess unique properties such as fractional electric charge, mass, and color charge. Quarks engage in all three fundamental

forces: weak, electromagnetic, and strong interactions. The color charge is a property exclusive to quarks and gluons that allows them to participate in the strong interaction. Quarks never exist in isolation due to a phenomenon known as confinement; instead, they combine to form hadrons. Hadrons are composite particles made up of quarks, which are bound together by the strong force, mediated by gluons 2.1.2. These particles are categorized into two main types based on their quark content and resultant spin: baryons and mesons. **Baryons**, such as the proton (uud) and neutron (udd), are composed of three quarks and are characterized as fermions with half-integer spins, following Fermi-Dirac statistics and obeying the Pauli exclusion principle. **Mesons**, on the other hand, are made of a quark-antiquark pair and have integer spin, classifying them as bosons that obey Bose-Einstein statistics and coexist in the same quantum state in large numbers. This complex behavior and interaction of quarks are essential to the formation and stability of matter, and they play a crucial role in the composition and characteristics of the universe.

- **Leptons**: Leptons are another group of half-spin elementary particles, distinct from quarks, but also coming in six types or flavors. Electrons, the most well-known leptons, are essential in forming atoms, while muons and tau particles are heavier with similar properties but shorter lifetimes. Their corresponding neutrinos are highly elusive because of their neutral charge and minimal interaction with matter which makes them hard to detect. Each lepton has a unique mass and an integer electric charge, except for neutrinos which are electrically neutral. Leptons interact through electromagnetic and weak forces, but unlike quarks, they do not participate in strong interactions.

2.1.2 Bosons - Force Carriers

On the other hand, bosons are a group of subatomic particles with integer spin that act as carriers of forces. In contrast to fermions which make up matter, they mediate interactions between other particles. The Higgs boson, an exceptional part of this group, plays a vital role in giving mass to other particles. Each type of boson is uniquely associated with a specific fundamental force:

- **Photon (γ)**: Photons carry the **electromagnetic force**, and are distinct in having no mass and traveling at the speed of light. In the electromagnetic force, particles with electric charge, such as electrons, interact through the exchange of photons.

- **Gluon (g)**: Gluons are massless gauge bosons and responsible for carrying the **strong nuclear force**. Strong force is the force that holds quarks together within hadrons, like protons or B mesons. This force is essentially the result of gluon interactions with quarks and other gluons, the particles with a special kind of charge called "color charge" (red, green, blue); however, this color is not a physical color seen by the eye but a metaphorical label. Only quarks and gluons carry this color charge, making them the exclusive participants in strong interactions. The strong force, mediated by gluons, ensures color charge is always conserved in a similar manner to how electric charge is conserved in electromagnetic interactions. As a result, gluons carry and exchange the color difference between quarks, as shown in Figure 2.2a. This process and all these rules are described by quantum chromodynamics (QCD).

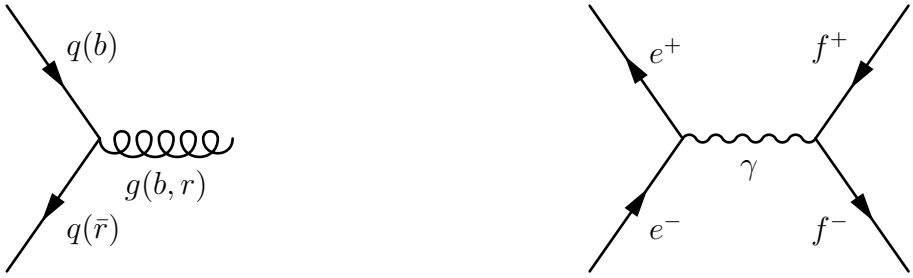

(a) Strong Interaction Mediated by g (b) Electromagnetic Interaction Mediated by γ

Figure 2.2: **Strong and Electromagnetic Interactions:** a) This subfigure depicts a strong interaction where a gluon (g) with color charges mediates two quarks. As it is shown, due to conservation of color charge, gluons carry two colors. b) It illustrates an electromagnetic interaction, with a photon (γ) mediating an electron and positron interacting to produce a charged fermion and anti-fermion pair.

- **W and Z**: The last force in the Standard Model, **weak nuclear force**, is mediated by W and Z bosons. This force is important for radioactive decay processes. There are two kinds of weak interactions: those involving $W^{\pm}$ bosons, and those involving the neutral Z boson. The former is either positively or negatively charged and can change one type of particle or flavor into another. However, the latter doesn't alter the type of the particles. Additionally, any interaction that a photon can mediate in electromagnetism, the Z boson can also mediate in the weak force. However, the key difference is that weak interaction violates parity (mirror symmetry), meaning the laws of physics do not remain the same by reversing spatial coordinates. These interactions can happen with both leptons and quarks, the counterparts possessing flavor charge. The weak interaction behaves differently for leptons and quarks, particularly in how it

affects their generation and flavor:

1. **Leptons**: For leptons, charged weak interactions mediated by $W^{\pm}$ bosons, can result in a change of flavor within the same generation[1]. For instance, an electron in an atom can be transformed into its neutrino during beta decay, while still remaining within the first generation of the leptons. As a result, lepton family numbers are conserved; electron number, muon number, and tau number are each preserved.
2. **Quarks**: On the other hand, in the case of quarks, quarks transition from one flavor to another, and crossing between generations is allowed. This is how a bottom quark (b) in a B^- meson ($b\bar{u}$) can change into a charm quark (c), leading to the B^- meson's transformation into a D^0 meson ($c\bar{u}$). Unlike leptons, quarks can change family identity, allowing for a mix between generations.

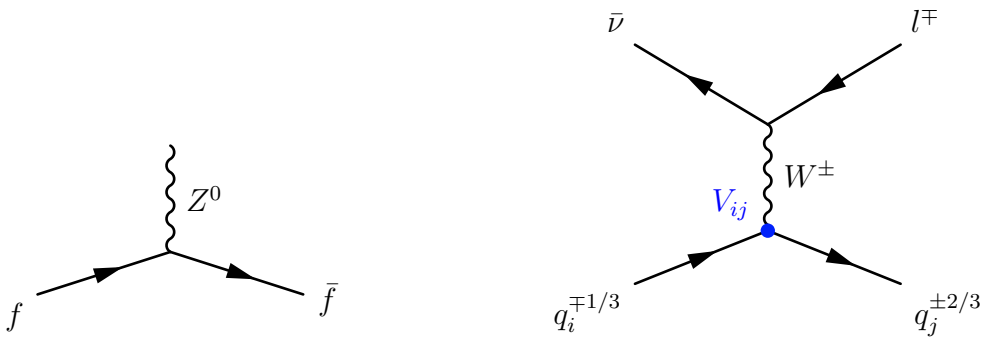

(a) Neutral Weak Interaction Mediated by Z^0 (b) Charged Weak Interaction Mediated by $W^{\pm}$

Figure 2.3: **Two Categories of Weak Interactions:** a) It illustrates a neutral weak interaction mediated by the Z^0 boson between two fermions f and $\bar{f}$. It exemplifies a process where a fermion and its corresponding antifermion interact without altering their flavor, as the Z^0 boson does not facilitate a change in quark generation or lepton type. As an example, the Z^0 boson can not mediate the interaction between two up-type quarks which have the same electric charge. b) This figure demonstrates a charged weak interaction mediated by the $W^{\pm}$ boson, separating the processes for leptons and quarks. For quarks, the diagram indicates a transition between up-type (q_j) and down-type (q_i) quarks, with the Cabibbo-Kobayashi-Maskawa (CKM) matrix element (V_{ij}) representing the probability amplitude for such a flavor change, which can be either in the same generation or cross generation (Section 2.3). However, for leptons, the generation change is not permitted within the Standard Model framework.

[1]It is not entirely accurate to say that leptons are unable to change generations. The primary goal of neutrino mixing experiments is to determine the elements of the PMNS matrix [8], which serves a similar role in the lepton sector as the CKM matrix (Section 2.3) does for quarks. However, this topic, which extends beyond the Standard Model, will not be explored further in this thesis.

Studying these particles gives us a deeper understanding of the fundamental structure and interactions within the universe

2.2 Discrete Symmetries In The Standard Model

In the Standard Model of particle physics, a variety of symmetries underpin the fundamental interactions and particles, one notable category is discrete symmetries, which include Charge Conjugation (C), Parity (P), and Time Reversal (T). Each of these symmetries, individually or in combination, is conserved or violated under different interactions.

- **Charge Conjugation (C)** refers to replacing a particle with its antiparticle, which possesses the same mass but opposite signed quantum numbers, like an electric charge.
- **Parity (P)** involves flipping the spatial coordinates (essentially, looking at the mirror image of a system). A violation of parity suggests that the laws of physics are not invariant under spatial inversion.
- **Time Reversal (T)** is a symmetry operation that inverts the direction of time, transforming a physical process to its mirror image in time, effectively reversing the sequence of events.

In the Standard Model, electromagnetic and strong forces conserve C, P and T symmetries, while the weak force violates both C and P individually and CP in combination. However, CPT theorem asserts that all physical processes are invariant under the combined operation of C, P and T symmetries. This means that when all three transformations are applied together, the laws of physics should remain unchanged.

CP violation is an observed phenomenon where the laws of physics do not apply equally to particles and their antiparticles when their spatial coordinates are inverted. This violation in weak interactions is important to explain why the universe is composed predominantly of matter, despite theoretical predictions that there should have been equal amounts of matter and antimatter produced during the Big Bang. The first observation of CP violation was made in experiments with neutral kaons in 1964 [9]

In the following section, the CKM matrix and its crucial role in CP violation will be explored, in addition to the importance of B meson decays in understanding and quantifying this phenomenon within the framework of the Standard Model.

2.3 CKM Matrix

In the framework of the Standard Model, quarks exist in two principal configurations: mass eigenstates and weak eigenstates. Mass eigenstates, such as u, c, t, d, s, and b quarks, are defined by distinct mass values that are known as flavors. During weak interactions, processes mediated by the $W^{\pm}$ bosons, quarks transform not strictly within the same family but through specific linear combinations of the down-type quarks (d, s, b), known as weak eigenstates (d', s', b') [10, p. 78]. In essence, the phenomenon of flavor changing in mass eigenstates allows for an up quark to form pairs or "doublets" not only with a down quark but also with strange and bottom quarks, thereby enabling transitions that span across different generations of quarks. Therefore, the generations grouped by quark masses do not align with the generations as defined by weak force interactions. Nonetheless, weak eigenstates of quarks can be established by transforming the mass eigenstates of down-type quarks into a new framework through a 3×3 matrix, known as the Cabibo-Kobayashi-Maskawa (CKM) matrix [11]. To ensure quark changes align with the concept of three families, different types of quarks (down, strange, and bottom) are mixed in a linear combination to make the weak eigenstates.

$$\begin{pmatrix} d' \\ s' \\ b' \end{pmatrix} = \begin{pmatrix} V_{ud} & V_{us} & V_{ub} \\ V_{cd} & V_{cs} & V_{cb} \\ V_{td} & V_{ts} & V_{tb} \end{pmatrix} \begin{pmatrix} d \\ s \\ b \end{pmatrix} \tag{2.1}$$

Now, weak eigenstates can be written as combinations of mass eigenstates through the equation below:

$$|b'\rangle = V_{td}\,|d\rangle + V_{ts}\,|s\rangle + V_{tb}\,|b\rangle$$

In this context, the weak interaction permits transitions only within these redefined groups:

$$\begin{pmatrix} u \\ d' \end{pmatrix}, \begin{pmatrix} c \\ s' \end{pmatrix}, \begin{pmatrix} t \\ b' \end{pmatrix}$$

Given that quarks are detected in their mass eigenstates, the experimentally observed probability for each type of weak transition reflects the degree of overlap between the mass and weak eigenstates. Notably, since the element V_{cb} of the CKM matrix is larger than V_{ub} by

an order of magnitude, it indicates that transitions from the charm quark to bottom occur more frequently than transitions from the up quark to the bottom quark [12].

$$|V_{\text{CKM}}| = \begin{pmatrix} 0.97435 \pm 0.00016 & 0.22500 \pm 0.00067 & 0.00369 \pm 0.00011 \\ 0.22486 \pm 0.00067 & 0.97349 \pm 0.00016 & 0.04182^{+0.00085}_{-0.00074} \\ 0.00857^{+0.00020}_{-0.00018} & 0.04110^{+0.00083}_{-0.00072} & 0.999118^{+0.000031}_{-0.000036} \end{pmatrix}$$

The CKM matrix, as a unitary matrix, can be parameterized in terms of four independent parameters. Three of these parameters can be chosen as real angles (θ_{ij}, i and $j = 1, 2, 3$ and they are indicating the generation numbers of the quarks), and the fourth parameter is a complex phase (δ) that introduces CP violation [12]. Moreover, a unitary matrix satisfies the following conditions [12]:

1. $\sum_i V_{ij} V_{ik}^* = \delta_{jk}$ for all j, k. This represents column-wise orthogonality.
2. $\sum_j V_{ij} V_{kj}^* = \delta_{ik}$ for all i, k. This represents row-wise orthogonality.

Here, V_{ij} is the amplitude for a transition from up-type quark q_j to down-type quark q_i, and δ_{jk} and δ_{ik} are Kronecher deltas. This unitary condition leads to a geometric representation known at the unitary triangle when plotted in the complex plane [13, p. 323] . This triangle is one of the six orthogonality conditions (e.g., $V_{ud}V_{ub}^* + V_{cd}V_{cb}^* + V_{td}V_{tb}^* = 0$), and has three interior angles labeled α, β, and γ. The values of these angles can be determined through experimental measurements of the CKM matrix elements [13, p. 322].

$$\alpha \equiv arg(-\frac{V_{td}V_{tb}^*}{V_{ud}V_{ub}^*}) \quad (2.2) \qquad \beta \equiv arg(-\frac{V_{cd}V_{cb}^*}{V_{td}V_{tb}^*}) \quad (2.3) \qquad \gamma \equiv arg(-\frac{V_{ud}V_{ub}^*}{V_{cd}V_{cb}^*}) \quad (2.4)$$

The measurements of the CKM matrix elements test if they fit within the expected theoretical framework. This involves checking if the constraints set by theory, such as those dictating that the sum of the interior angles of the unitary triangle should equal 180 degrees, hold true in practice.

2.4 B Mesons

Among the array of mesons predicted by the Standard Model, B mesons stand out for their critical role in particle physics research, particularly in the context of electron-positron collider experiments known as B-factories such as Belle, Belle II, and BaBar [14], the Belle

II experiment will be discussed with more details in Chapter 3. Although each e^-e^+ collider experiment was designed with its own unique objectives, the underlying motivation for many of them was the discovery and measurement of CP violation in the B meson system, a milestone achievement first observed independently in neutral B mesons by the Belle and BaBar in 2001 [15, 16].

The B^+ and B^0 mesons are composed of a bottom anti-quark ($\bar{b}$) bound to an up (u) or down (d) respectively through strong interaction, while their antiparticles, B^- and $\bar{B}^0$, contain a bottom quark (b) coupled with an anti-up ($\bar{u}$) or anti-down ($\bar{d}$) quark. B mesons also include versions with strange (s) or charm (c) quarks to create B_s^0 ($s\bar{b}$) and B_c^+ ($c\bar{b}$), which complete the B-meson family. B mesons can decay through numerous allowed decay channels [17], each characterized by its branching fraction, which represents the proportion of total decays that occur via a specific mode. These decay processes are classified into three distinct categories: leptonic, hadronic, and semileptonic B meson decays (Figure 2.4).

Semileptonic B Decays

The most common decay paths for B mesons involve flavor-changing charged current processes, where a bottom anti-quark ($\bar{b}$) turns into either a charm ($\bar{c}$) or an up anti-quark ($\bar{u}$). Semileptonic decays, represented as $\bar{b} \to \bar{c}(\bar{u})l^+\nu$ (where l stands for lepton: electron e, muon μ or tau τ), play an important role in these studies.These decays are particularly interesting because they allow for precise measurement of the elements of the CKM matrix, especially $|V_{cb}|$ and $|V_{ub}|$, which are essential for understanding quark mixing and CP violation [18].

To determine $|V_{cb}|$ and $|V_{ub}|$, two main experimental approaches are utilized. The first involves exclusive semileptonic B decay, focusing on final states where the hadronic system consists of specific particles like D, D^*, D^{**}, π, or ρ mesons. This method allows for targeted study of specific decay channels. The second approach examines inclusive semileptonic decays, where B mesons decay into a broad spectrum of hadronic states, denoted as X_c or X_u depending on whether the final state includes a charm or an up quark (Figure 2.4c).

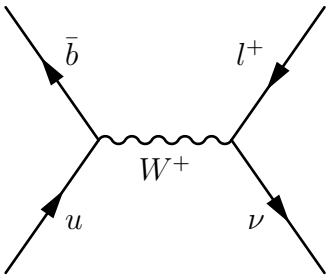

(a) Leptonic B Meson Decay: $B^+ \to l^+\nu$

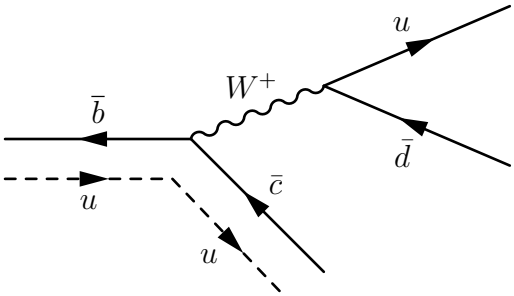

(b) Hadronic B Meson Decay: $B^+ \to \bar{D}^0\pi^+$

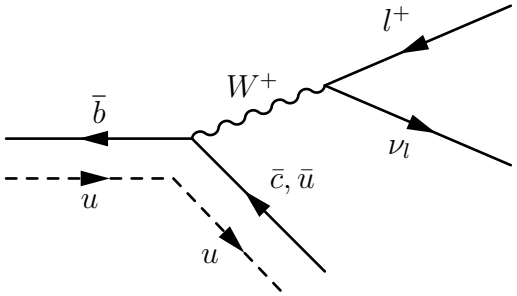

(c) Semileptonic B Meson Decay: $B^+ \to X_{c(u)}l^+\nu$

Figure 2.4: **Categories of B meson Decays:** a) Leptonic decay, with the B meson decaying entirely into leptons; b) Hadronic decay, where the B meson decays into purely hadronic final states; and c) Semileptonic decay, featuring a B meson decaying into a combination of hadronic and leptonic final states.

2.5 Feasibility Study for Measuring the $B^- \to D^{(*)0}\eta\ell^-\bar{\nu}$ Branching Fraction

The primary objective of this thesis is to investigate the branching fraction of the rare semileptonic decay mode $B^- \to D^{(*)0}\eta\ell^-\bar{\nu}$ [2]. This decay channel is particularly interesting due to its potential to shed light on the difference known as the "gap problem" within B meson decay studies. This problem is characterized by the observed divergence between the overall inclusive semileptonic branching fraction and the summed branching fraction of exclusively measured decay modes for semileptonic B decays, as demonstrated by equation 2.5.

$$\mathcal{B}(B^+ \to X_c\ell^+\nu) = (10.90 \pm 0.14)\% \neq \sum_{i=D,D^*,D^{**}} \mathcal{B}_i(B^+ \to X_c^i\ell^+\nu) = (9.2 \pm 0.2)\% \text{ [19]} \quad (2.5)$$

[2] **What is An Eta Meson?** The eta (η) meson is a neutral meson composed of a mixture of up, down, and strange quark-antiquark pairs ($\frac{1}{\sqrt{6}}(u\bar{u} + d\bar{d} - 2s\bar{s})$). It is part of the pseudoscalar meson family, which means it has a spin (J) and isospin (I) of 0, and odd parity. The specific mixture of quark-antiquark pairs in the η results in a cancellation of isospin contributions. Its mass is approximately 547.862 MeV, and it decays promptly into a pair of photons ($\gamma\gamma$) or three pions ($\pi^0 + \pi^0 + \pi^0$ or $\pi^+ + \pi^0 + \pi^-$).

By examining the $B^- \to D^{(*)0}\eta\ell^-\bar{\nu}$ decay pathway, this analysis aims to explore the possibility that this channel contributes to the unexplained portion of the inclusive semileptonic branching fraction, thereby offering a potential solution to bridge the gap between exclusive and inclusive measurements.

CHAPTER 3

Experimental Setup

This chapter will cover the Belle II experiment and how its sub-detectors function. Each subdetector including tracking detectors that follow the paths of charged particles, calorimeters for measuring energy, and others is designed to detect and measure specific types of particles created during e^+e^- collisions [6]. Understanding the design of the sub-detectors is crucial for interpreting the data coming from Belle II.

3.1 SuperKEKB and Belle II Experiment

Collisions in particle physics are essential because they enable the study of particles that are otherwise invisible and inaccessible. These high-energy collisions facilitate the exploration of unknown phenomena and the potential discovery of new particles, furthering the understanding of the physics laws. To achieve that, particles must be accelerated to gain enough energy to produce heavy and naturally difficult-to-observe particles with short lifetimes, such as $B\bar{B}$ meson pairs. SuperKEKB is a high-energy particle accelerator in Japan, designed to collide e^- and e^+ at an energy level of $\sqrt{s} = 10.58\ GeV$ [5]. The process of electron-positron annihilation into an Upsilon(4S) particle begins as follows:

$$e^+e^- \rightarrow \Upsilon(4S) \tag{3.1}$$

The conservation of the four-momentum of the particles:

$$\begin{aligned} &\mathrm{P}_{e^+} + \mathrm{P}_{e^-} = \mathrm{P}_{\Upsilon(4S)} \\ &\mathrm{M}^2_{e^+} + \mathrm{M}^2_{e^-} + 2\ \mathrm{E}_{e^+}\mathrm{E}_{e^-} - 2\ |\vec{\mathrm{p}}_{e^+}||\vec{\mathrm{p}}_{e^-}| \cos\theta_{e^+,e^-} = \mathrm{M}^2_{\Upsilon(4S)} \end{aligned} \tag{3.2}$$

It is assumed that the masses of e^+ and e^- are negligible, equating their energies to their momenta. Additionally, as they move in opposite directions, the angle between them is approximately 180°. The SuperKEKB collider features two separate rings: one for 7-GeV

electrons, known as the High-Energy Ring (HER), and another for 4-GeV positrons, called the Low-Energy Ring (LER)[20]. So,

$$E_{\text{CMS}} = 2\sqrt{E_{\text{HER}}\ E_{\text{LER}}} = 10.58\ \text{GeV} = M_{\Upsilon(4S)} \tag{3.3}$$

This energy in the Central Mass System (CMS) is specifically chosen to maximize the production of e^+e^- collisions that lead to an $\Upsilon(4S)$ resonance. The $\Upsilon(4S)$ is a specific resonance, a state where particles can exist briefly before decaying. The upsilon meson is the bound state of a bottom quark (b) and its antiparticle ($\bar{b}$), and the '4S' designation refers to its energy level and orbital angular momentum properties. It is called a "resonance" in particle physics because it is a temporary state formed when particles like quarks briefly bind together and then quickly fall apart again. The $\Upsilon(4S)$ meson predominantly decays into B mesons pairs ($B\bar{B}$), with a branching fraction of over 96%. The energy chosen to produce $\Upsilon(4S)$ in the Belle II experiment is set slightly above the threshold required for the creation of $B\bar{B}$ pairs (B^+B^- and $B^0\bar{B}^0$), with no additional particles, as displayed in Figure 3.1. Operating at an energy slightly above the threshold for $B\bar{B}$ pair production ensures that the B mesons four-momenta sum to the initial state four-momenta. This careful calibration of energy prevents the production of other particle types while allowing properties such as momentum and energy of one B meson to be inferred from the decay of its entangled partner ($\bar{B}$).

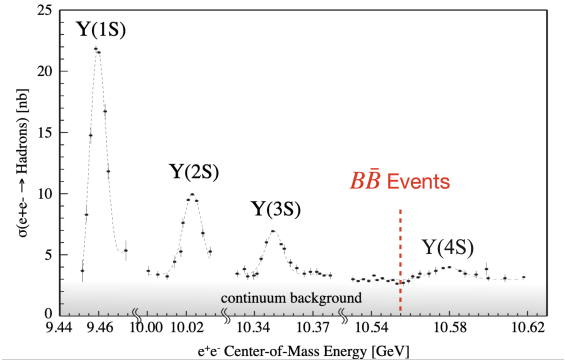

Figure 3.1: **Invariant Mass of electron-positron Annihilation** - Energy spectrum illustrating the production cross-section of e^+e^- collisions resulting in hadrons, with distinct resonance peaks for Υ states and $B\bar{B}$ production threshold, against a continuum background for lighter quarks (u, d, s, c) [21].

Eq. 3.4 expresses the relativistic energy and momentum, where E (eV) is the energy of a particle, p (eV/c) is the momentum, γ is the Lorentz factor, m (eV/c^2) is the mass of the

particle, and c (m/s) is the speed of light. This equation shows how the energy of a particle increases as its speed approaches the speed of light:

$$E \equiv \gamma mc^2 \tag{3.4a}$$

$$p \equiv \beta\gamma mc \tag{3.4b}$$

The Lorentz factor describes how energy, momentum, and relativistic mass change for an object moving at the velocity v relative to c. Here β is the velocity of the particle as a fraction of the speed of light.

$$\gamma = \frac{1}{\sqrt{1-\beta^2}}, \qquad \beta \equiv \frac{v}{c} \tag{3.5}$$

Rearranging the given equations leads to the Lorentz boost factor, which quantifies the change in energy and momentum of the produced particles in the collider.

$$\beta\gamma = \frac{p}{mc} \tag{3.6}$$

Asymmetric energies of e^- and e^+ rings (7 (GeV) and 4 (GeV), respectively) result in a Lorentz boost Eq. 3.6, causing the B mesons produced in the collision to travel in the direction of the higher-energy beam. Therefore, the center of mass of the annihilation is not stationary in the lab frame. In fact, the boost increases the decay length of unstable particles. As a result, the B meson pairs will travel a longer distance before decaying into other particles, making it possible to measure the distance traveled in the lab.

In the center of mass frame of $\Upsilon(4S)$, where the momentum of Upsilon meson is zero, the momentum of B and $\bar{B}$ are as follows:

$$\vec{p}_B = -\vec{p}_{\bar{B}}$$

$$p_B^{CMS} \equiv |\vec{p}_B| = |\vec{p}_{\bar{B}}| = \sqrt{\frac{M^2_{\Upsilon(4S)}}{4} - M_B^2} \approx 0.341 \text{ (GeV/c)} \tag{3.7}$$

Inserting the known values for p_B^{CMS} and the rest mass m_B of the B meson in equation 3.6, the speed β_B^{CMS} is found to be 0.064. Moving to the lab frame, $\Upsilon(4S)$ possesses a non-zero momentum ($p^{lab}_{\Upsilon(4S)}$) of 3 (GeV/c) due to the asymmetric energy of the colliding beams, which corresponds to a velocity ($\beta^{lab}_{\Upsilon(4S)}$) of 0.27 when considering its rest mass. The goal is to determine the decay length (l) of B and the $\Upsilon(4S)$ mesons in the lab frame, which requires

the particle's momentum in that frame. The momentum of the $\Upsilon(4S)$ is already known, leading to a calculated decay length of 2.7×10^{-29} microns in the lab frame. To calculate the momentum of B mesons in the lab frame, it is necessary to know their velocity in the lab frame. To obtain the velocity of the B meson in the lab frame, a Lorentz transformation is employed, incorporating the known velocity of the $\Upsilon(4S)$ in the lab frame along with the B meson's velocity in the CMS. Taking as an example where the B velocity in the $\Upsilon(4S)$ frame is orthogonal to the boost direction, the Lorentz transformation facilitates the calculation of the B meson's velocity in the lab frame (β_B^{lab}) to be 0.28, as it is shown in equation 3.8, which accordingly yields a momentum (p_B^{lab}) of 1.53 (GeV/c).

$$\mathbf{v}_B^{lab} = \frac{1}{1 + \frac{\mathbf{v}_{\Upsilon(4S)}^{lab} \cdot \mathbf{v}_B^{CMS}}{c^2}} \left[\frac{\mathbf{v}_B^{CMS}}{\gamma_{\mathbf{v}_{\Upsilon(4S)}^{lab}}} + \mathbf{v}_{\Upsilon(4S)}^{lab} + \frac{1}{c^2} \frac{\gamma_{\mathbf{v}_{\Upsilon(4S)}^{lab}}}{\gamma_{\mathbf{v}_{\Upsilon(4S)}^{lab}} + 1} (\mathbf{v}_B^{CMS} \cdot \mathbf{v}_{\Upsilon(4S)}^{lab}) \mathbf{v}_{\Upsilon(4S)}^{lab} \right] \tag{3.8}$$

While we are unable to directly measure where the B mesons are produced, we can calculate where they decay. This decay point gives us the mesons' travel distance in the lab, which is calculated in Eq. 3.9. In this formula l is the distance the B meson travels before decaying, p and m are the momentum and mass respectively, c is the speed of light, and τ is the proper time; proper time is the time interval measured by the clock that is at rest relative to the event being observed, essentially the actual time as experienced by the object in its rest frame.

$$l_i^{lab} = \frac{p_i^{lab}}{m_i c} c\tau_i \tag{3.9}$$

Charged B meson has a lifetime of roughly 1.6 ps, therefore the decay length will be approximately 140 μm (Table 3.1). However, if the beam energies were equal, the momentum of $\Upsilon(4S)$ would be zero in the lab frame, and the B meson produced would have the momentum value they inherently possess in the $\Upsilon(4S)$ rest frame, without any additional momentum from the movement of the $\Upsilon(4S)$ itself. Consequently, the decay length of charged B meson at $\Upsilon(4S)$ rest frame is approximately 30 μm, which is nearly five times shorter than its decay length in the lab frame at SuperKEKB. Therefore, the boost makes B mesons travel further before decaying, which helps in taking advantage of unequal-energy beams to better observe their behavior.

Table 3.1: **B Mesons Decay Lengths** - A summary of the key features of the B mesons and $\Upsilon(4S)$, and their decay lengths in the lab frame.

Particle	**Content**	**Isospin** I^G or I	**Spin and Parity** J^{PC} or J^P	**Rest Mass** (GeV/c^2)	**Decay Length** (μm)
$\Upsilon(4S)$	$b\bar{b}$	0^-	1^{--}	10.579	2.7×10^{-9}
B^+	$u\bar{b}$	$\frac{1}{2}$	0^-	5.279	142.9
B^0	$d\bar{b}$	$\frac{1}{2}$	0^-	5.279	132.3

3.2 Superconducting Solenoid

The superconducting solenoid occupies the space between ECL (section 3.3.4) and KLM (section 3.3.5) detectors, producing a uniform 1.5 T magnetic field across a cylindrical volume of 4.4 m in length and 3.4 m in diameter. When a magnetic field is generated in a solenoid, the magnetic field lines travel from one end of the solenoid to the other, both inside and outside the coil. However, to maintain a strong and uniform field inside the detector and to reduce stray magnetic fields outside (which can interfere with other equipment or experiments), it is beneficial to provide a path for the magnetic flux to "return" through a material that easily conducts magnetic fields. Magnetic flux return is achieved by surrounding the solenoid with high magnetic permeability material, such as iron in the KLM, which provides a low-resistance path for magnetic field lines to complete their loop. This method channels the magnetic flux, enhancing the magnetic field's effectiveness in the needed areas and reducing stray fields [22].

3.3 Belle II Subdetectors

The Belle II detector shown in Figure 3.2 is a complex assembly of various sub-detectors. At its core, Belle II features a layered design, starting from the interaction point where particle collisions occur and extending outward. Each layer is specialized for detecting specific types of particles or measuring particular properties, such as their charge, momentum, energy, or identity. The Belle II experiment utilizes Cartesian and spherical coordinate systems with the interaction point (IP) as the origin. In Cartesian coordinates, the positive z-axis points along the electron beam's direction, dividing the space into a forward (positive z) and a

backward (negative z) region. The y-axis is vertical, with increasing y values indicating greater elevation. Conversely, the x-axis extends horizontally away from the center of the accelerator ring. For spherical coordinates, the radius (r) measures the distance from the origin, the polar angle (θ) is measured from the z-axis, and the azimuthal angle (ϕ) is measured from the x-axis. In the following sections, each part of the Belle II detector will be explored in detail, highlighting its unique functions.

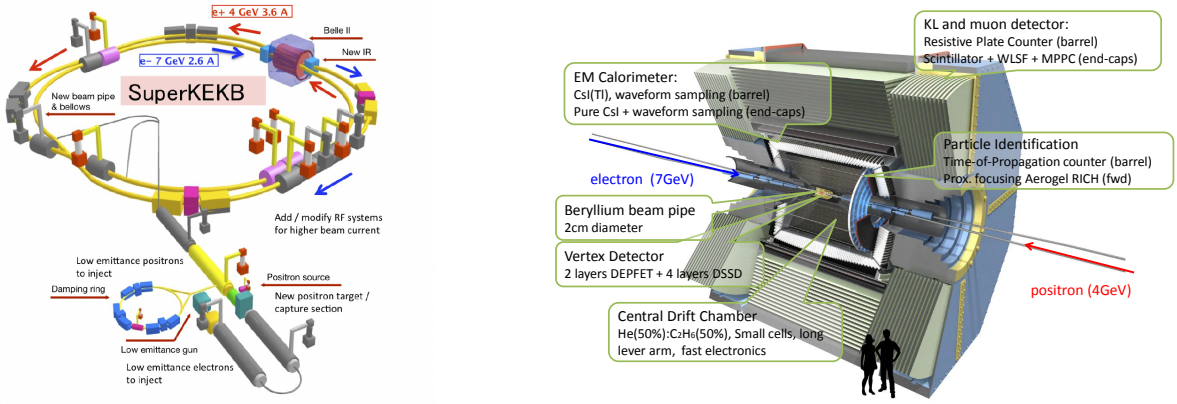

Figure 3.2: **SuperKEKB Accelerator and Belle II Detector** - Cross-sectional diagram of the Belle II detector showing the various components including a short description of each sub-detector, with the trajectories of electron and positron beam pipes [23].

3.3.1 Vertex Detector

The first sub-detector in Belle II is the vertex detector, responsible for precisely identifying the vertices where particles collide and subsequently decay. It is positioned closest to the interaction point (IP), enabling it to accurately determine the locations of the interactions. By measuring where particles come from and where they decay, the vertex detector provides essential information tracing the paths and understanding the behaviors of particles. This is especially important for studying short-lived particles, like B mesons, which decay near their point of origin. This sub-detector is made up of two parts: the Pixel Detector and the Silicon Vertex Detector.

Pixel Detector (PXD)

The first component is the pixel detector located 14 mm away from the IP. It consists of two layers equipped with advanced DEPFET[1] sensor technology. These sensors are highly

[1]Depleted Field Effect Transistor [5]

resilient to the intense radiation environment near the IP, making them suitable for the first layers where the particle activity is greatest. When particles travel through any material, they can be deflected or scattered, altering their original paths. DEPFET technology allows for the construction of exceptionally thin sensors, approximately 50 microns in thickness. This reduced thickness is crucial as it minimizes the impact of multiple Coulomb scattering on the trajectories of the particle, thereby enhancing the precision of the measurements. The PXD is composed of pixelized panels that accurately determine particle decay positions with a resolution of around 10 microns. Additionally, these panels have advanced readout electronics, which can digitize pixel data in just about 20 microseconds for efficient data processing.

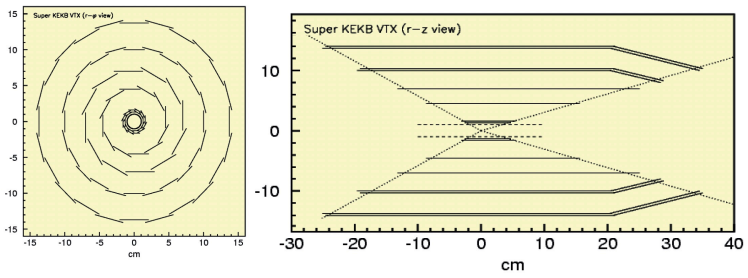

Figure 3.3: **Vertex Detector** - Schematic representation of the SuperKEKB Vertex Detector with two layers of PXD and four layers of SVD. The left image illustrates the detector's circular layering in the horizontal plane, and the right image depicts the vertical cross-section [6].

Silicon Vertex Detector (SVD)

Positioned just outside the PXD, the silicon vertex detector (SVD) has four layers, each with double-sided silicon strip detectors (DSSDs)[5], as it is demonstrated in Figure 3.3. Layers of PXD and SVD are key in tracking the paths of charged particles. As these particles traverse the SVD, they ionize the silicon, resulting in electron-hole pairs that generate detectable signals. Unlike the PXD, which employs pixelized sensors for high-precision measurements in both x and y directions, the SVD utilizes silicon strips. This configuration leads to good precision along one axis, making it less detailed compared to the pixelized approach of the PXD but still effective over a larger area. This design choice balances cost and performance, allowing for efficient tracking and measurement of the spatial location of charged particles at a slightly greater distance from the IP.

3.3.2 Central Drift Chamber (CDC)

After the SVD and PXD, there is the central drift chamber (CDC). The CDC is a large cylindrical chamber that is filled with gas and has over 14,000 sensing wires arranged in 56 layers and 42,240 field wires. These wires are split into anode wires (connected to a positive high voltage) and cathode wires (grounded). The central drift chamber has three key functions:

1. It tracks the paths of charged particles and accurately measures their momentum and the time difference of the drift from where they come and where they are detected.

2. It helps identify what type of particles they are by looking at how much energy they lose as they travel through the gas in CDC, which is particularly valuable for low-momentum tracks that elude other identification devices.

3. It generates reliable trigger signals for the presence of charged particles

- **Electric Field**: The electric field in the CDC was created by applying a voltage difference between the anode and cathode, which serves two primary functions. When charged particles pass through $He - C_2H_6$, they knock electrons off the gas molecules along their path. The liberated electrons drift towards the positively charged wires, while the positive ions move towards the negatively charged wires. This movement is crucial for detecting the presence and location of the ionization events, as the electrons reaching the anode wires produce electrical signals. These electrical signals are processed to reconstruct the path of the charged particles. This reconstruction is based on the location and timing of the signals along the wires. Moreover, the local electric field induced by the field wires accelerates these free charges. The accelerated charges gain enough energy to ionize more gas molecules, creating even more free electrons and ions. This chain reaction leads to a significant increase in the number of free charges, therefore an amplification of the signal.

- **Magnetic Field**: In addition to the electric field, as charged particles move through the CDC, they encounter the 1.5 T Belle II detector magnetic field, as was previously explained in section 3.2. This field exerts the Lorentz force perpendicular to their direction of motion and the magnetic field's direction. The force causes the charged particles' trajectories to bend or curve. The nature of this curvature is governed by the particle's charge (positive or negative) and its momentum. The amount of curvature in a particle's path is inversely proportional to its momentum. Therefore,

the magnetic field's strength and the curvature radius provide data to determine the particle's momentum.

In summary, combining information about the curvature of the particle's path and the rate of energy loss in the chamber can identify the type, charge, and momentum [5].

3.3.3 Particle Identification (PID)

In high-energy settings, differentiating between charged particles moving at or greater[2] than the speed of light can be challenging, particularly when these particles leave similar tracks in detectors such as the CDC. Kaons ($K^{\pm}$) and pions ($\pi^{\pm}$) are examples of such particles that often travel at these high speeds and can produce indistinguishable tracks in the CDC. To address this, the Particle Identification Detectors (PID) provide a solution. The PID subsystem in Belle II distinguishes various types of charged particles by measuring their velocity. It comprises two separate Cherenkov detectors: the Time Of Propagation (TOP) detector and the Aerogel Ring Imaging CHerenkov (ARICH) detector. Cherenkov radiation is a phenomenon that occurs when a charged particle travels through a medium at a speed greater than the phase velocity of light in that medium. This results in the emission of a faint, blue-tinged light, analogous to a sonic boom but with light.

Time Of Propagation (TOP)

The TOP detector is situated in the barrel region, encircling the CDC. It consists of 16 large quartz bars, which serve as the medium for Cherenkov radiation. The emitted Cherenkov light is internally reflected within the bars and directed toward the end, where it is detected by the readout system. This system includes two rows of sixteen micro-channel plate photomultiplier tubes (MCP-PMTs). Additionally, focusing mirrors are employed at the other end of each bar to aid in directing the light toward the detectors.

[2]Speed of light is approximately 3×10^8 m/s in a vacuum, represents the ultimate speed limit, beyond which no object or signal can travel; However, at high energies, particles can exceed the phase velocity of the light in a medium such as water, where the light travels at a reduced speed, typically about 75% of its speed in a vacuum

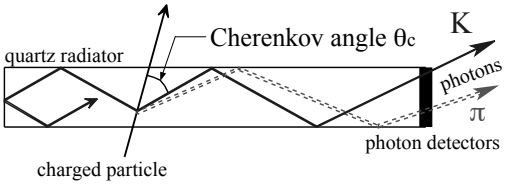

Figure 3.4: **Particle Identification, TOP** - Schematic of Cherenkov radiation within the TOP detector. A charged particle moving through a quartz radiator emits photons at the Cherenkov angle θ_c, which are then directed towards the photon detectors [5, p. 220].

The TOP precisely measures the time of arrival and the position where these photons hit the MCP-PMTs. From these measurements, the Cherenkov cone's angle is determined. The Cherenkov light emitted by particles like pions and kaons travels different path lengths to the photon detectors due to their slight angular differences, leading to variations in the timing of light arrival. This capability allows minor differences in timing to be detected, to determine whether the charged particle's trajectory originated from a pion or a kaon. As it is shown in Eq. 3.10, the Cherenkov angle (θ_c) depends on the velocity of the particle (β) and the refractive index of the quartz (n).

$$cos\theta_c = \frac{1}{n\beta} \tag{3.10}$$

By combining the information about the particle's velocity in TOP and the particle's momentum in CDC using formula 3.6, the mass of the charged particle will be reconstructed revealing the type of the particle.

Aerogel Ring Imaging CHerenkov (ARICH)

Located in the forward endcap region beyond the CDC, the ARICH detector also uses Cherenkov radiation to enhance the particle identification capabilities of the TOP. The ARICH detector features aerogel rings as its central component, where Cherenkov photons are generated as charged particles move through the aerogel faster than light travels in it. Aerogel is chosen for its low refractive index, amplifying the Cherenkov effect's sensitivity to fast-moving particles. The relationship $cos(\theta_c) = \frac{1}{n\beta}$ illustrates that a lower refractive index (n) allows for the distinction of particles with minor velocity differences through significantly varying Cherenkov angles (θ_c). As illustrated in the schematic side view of the ARICH in Figure 3.5, the aerogel rings consist of two layers with different refractive indices: 1.045 for the upstream layer and 1.055 for the downstream layer. These layers are set up so that the light beams from both layers come together at the same spot on the detector's reading area.

Following the aerogel rings, an expansion volume provides space for the photons to disperse into a cone formation. Around this space, the hybrid avalanche photon detectors (HAPD) are arranged in circles to find out roughly where the light hits. The radius of the ring pattern onto the detector plane is directly related to the Cherenkov angle, which depends on the velocity of the particle and the refractive index of the aerogel.

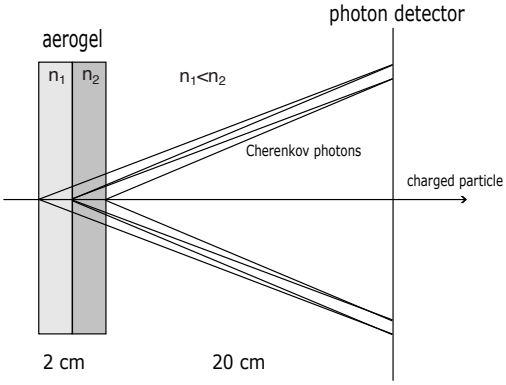

Figure 3.5: **Particle Identification, ARICH** - Diagram illustrating the operation of the ARICH detector. A charged particle passes through a dual-layer aerogel radiator, emitting Cherenkov photons at different angles due to the varying refractive indices (n1, n2), which are then captured by the photon detector after traveling a 20 cm expansion volume. [5, p. 251]

In summary, for low momentum particles, the time difference[3] is a sufficient and effective method for PID because the variation in travel times is significant enough to distinguish between different types of particles. However, for high-momentum particles, where the time differences become too small due to their near-light speeds, Cherenkov radiation in TOP and ARICH provides a more effective means of identification by exploiting the velocity-dependent properties of this radiation.

3.3.4 Electromagnetic Calorimeter (ECL)

The Electromagnetic CaLorimeter (ECL), positioned outside the TOP and ARICH detectors, encompasses three distinct sections: the barrel, the forward, and the backward endcap. Therefore, it effectively covers a wide polar angle range. The ECL is constructed from dense scintillating thallium-doped cesium iodide CsI(Tl)crystals. One of the main functions of the ECL is to detect photons and electrons and accurately measure their energy deposit.

[3]The difference in time between the particle's creation and its detection by the PID system. Also known as Time of Flight.

Additionally, given the known collision region of the beams and the known impact location on the crystal, the particle's direction of travel from the IP can be inferred. This level of precision is vital for the reconstruction of decay products from B mesons, including π^0 and D^* mesons, which emit photons across a diverse energy spectrum. Moreover, the Belle II calorimeter has the advanced capability to distinguish between two main types of particle showers (electromagnetic showers and hadronic showers). **Electromagnetic showers** are generated by electrons, positrons, or photons interacting with the matter, leading to a dense cascade of secondary particles. These showers are characterized by their compactness and uniform energy deposition. In contrast, **hadronic showers** are produced by hadrons and involve both electromagnetic processes and strong nuclear interactions. This results in a more extensive and less uniform energy spread. The light generated from these energy depositions is captured by photodiodes attached to the crystals; the light collected is proportional to the particle energy. This process enables the identification and allows for the measurement of the energy from both charged and neutral particles. It also contributes to the detector's trigger decision process about which events the detector should record.

3.3.5 K_L^0 and μ Detector (KLM)

The KLM detector, positioned as the outermost sub-detector in the Belle II setup, is tasked with identifying muons (μ) and long-lived neutral kaons (K_L^0). The KLM detector utilizes Resistive Plate Chambers (RPCs), which are composed of layers including electrodes, gas-filled regions, and insulators. In addition to RPCs, iron plates are incorporated to fulfill critical roles. These iron plates are instrumental in providing a magnetic field flux return, improving the efficiency of the superconducting solenoid's magnetic field within the detector. They also increase the probability of interactions with neutral particles (K_L^0) by offering a dense material for such interactions to occur, including nuclear capturing[4]. This dual functionality not only optimizes the detector's sensitivity and precision in particle detection but also contributes to shielding capabilities [5].

Muons, elementary particles with properties similar to electrons but significantly heavier (207 times the m_{e^-}), are capable of traversing matter with minimal energy loss, allowing

[4]The neutral particle can be absorbed by the nucleus within the material, in KLM case iron, leading to nuclear reactions. This process often results in the production of secondary particles.

them to penetrate deeply into dense material. K-Long is a mass eigenstate[5] of neutral kaon, mostly decaying into three pions, and having a longer lifetime. They live long enough to pass through the initial detectors without interacting. Other particles, such as electrons, protons, and charged pions, are stopped or absorbed within the inner layers due to their strong interactions with the detector material. Electrons, for instance, lose energy rapidly through bremsstrahlung and ionization processes, while protons and charged pions undergo nuclear interactions and scattering, preventing them from reaching the outer layers like the KLM detector. Photons are also absorbed or scattered by interactions such as pair production and Compton scattering within the calorimeter.

When charged particles, μ or the decay products of K_L^0 mesons, pass through these RPCs, they ionize the gas within, and an electric field accelerates the resulting electrons to produce a detectable signal. For muons, which retain their energy through earlier detector layers, the KLM uses hits aligned with the extrapolated path from the CDC to pinpoint their presence. As for K_L^0 mesons, the KLM identifies them by forming clusters of hits in its active layers, where the absence of an associated track from charged particles suggests the presence of these neutral mesons. However, these clusters primarily give directional information of the K_L^0 candidates rather than precise energy levels, as the number of hits can vary.

All in all, the accurate detection of muons is achieved by correlating the signal location in KLM with the CDC's track data. Moreover, the directional resolution of K_L^0 can be enhanced when clusters detected by the KLM can be associated with corresponding clusters in the ECL.

3.4 Data Acquisition and Trigger

In the high-intensity environment of the Belle II detector, data is generated at an extraordinary rate, with several hundred-kilo channels outputting information approximately every 8 (ns). Data is temporarily held in a buffer for a mere 5 microseconds before the oldest data is overwritten by new information. As discussed previously, each sub-detector has a specialized function and contributes specific information to the trigger decision process. They each have their own set of criteria to quickly assess whether the signals they detect might indicate a significant physics event.

[5]Neutral kaons (K^0) and their antiparticles ($\bar{K^0}$) can transform into each other through weak interaction processes. The weak interaction allows for the phenomenon of particle-antiparticle mixing, where K^0 and $\bar{K^0}$ can oscillate between each other. This mixing leads to two distinct physical states that have definite lifetimes and decay modes. Therefore, the actual particles observed in experiments are not directly the K^0 and $\bar{K^0}$ as produced, but rather their quantum superposition. The two superpositions of K^0 and $\bar{K^0}$, also known as weak eigenstate, are K_L^0 and K_S^0

Although all subdetector components are equipped with Field-Programmable Gate Arrays (FPGAs), they are unable to independently identify events pertinent to physics. Therefore, Belle II employs a sophisticated two-tiered trigger system for data acquisition and analysis. The initial stage is the Level-1 (L1) trigger, implemented on FPGAs, which rapidly assesses the data stream to identify potentially significant events at rates up to 30 kHz. The L1 trigger system interfaces directly with the detector's front-end electronics, which are strategically situated in proximity to, or within, the detector apparatus to ensure minimal signal degradation.

Table 3.2: **Subdetector Contributions Trigger Decisions** - A summary of the specific trigger decision parameters contributed by each sub-detector. The Particle Identification (PID) system provides timing information, the Central Drift Chamber (CDC) supplies data on momentum, position, and charge of charged particles, the Electromagnetic Calorimeter (ECL) determines the size and position of energy deposits, and the K_L^0 and μ detector (KLM) identifies muon and long-lived kaon tracks, each critical for the trigger decision process.

PID	CDC	ECL	KLM
time	momentum, position, charge	size and position	μ and K_L^0
of particle interaction	of charged particle	energy deposits ($\frac{dE}{dx}$)	tracks

Once an event passes the level 1 (L1) trigger, the corresponding data is promptly digitized and buffered from each sub-detector, then coherently assembled by the event builder. This assembled event undergoes further filtering by the High Level Trigger (HTL), a network of computers that execute detailed event reconstruction and selection algorithms. Events deemed scientifically relevant by the HTL are then committed to permanent storage for offline analysis [24, 25].

3.5 Simulation and Monte Carlo (MC)

Unlike real data, which is collected from physical particle collisions within the detector, Monte Carlo (MC) simulations are computer-generated datasets that mimic these collisions based on theoretical models. Event simulation begins by generating decay events, such as those from an $\Upsilon(4S)$ particle, based on theoretical physics models. These models range from

Standard Model processes to SUSY[6] and dark matter scenarios. Particle event generation involves creating particles' positions and four vectors according to the chosen model, a task performed by various event generators such as EvtGen [27], tailored to specific physics processes or analysis needs ($\Upsilon(4S)$ decays, B meson decays, e^+e^- to $q\bar{q}$ annihilation). This stage is independent of the detector's specifics and focuses solely on the theoretical aspects of particle physics. Following event generation, the most well-known simulation software, Geant4 [28], simulates the interaction of these particles with the virtual Belle II detector, accurately modeling physical phenomena like ionization and Cherenkov radiation to produce realistic detector responses. This detailed simulation process, which translates theoretical particle events into expected detector signals, is computationally intensive, taking up to a second per event for Belle II, and significantly longer for experiments at higher energies like ATLAS.

3.6 The Belle II Analysis Software Framework (BASF2)

After collecting raw data from the detector and generating corresponding simulated data, both datasets undergo calibration and are then stored at the KEK computing center. To manage the vast volume of data and computational demands, a global grid computing network is utilized, allowing for efficient parallel processing. The refined data is then stored in condensed mDST files. The Belle II Analysis Software Framework (BASF2) provides a unified environment for both the simulation of particle physics events (using Monte Carlo techniques) and the analysis of real data collected by the detector. This consistency ensures that the tools and methods developed for analyzing simulations are directly applicable to the real experimental data. For targeted analysis, derived ntuple-files are generated from the mDSTs using BASF2. These subsequent files are tailored datasets containing event variables structured for efficient access and manipulation, thus streamlining the final stages of the physics analysis pipeline.

[6]Supersymmetry (SUSY) is a theoretical framework that proposes a type of symmetry connecting bosons and fermions, suggesting that each particle has a corresponding partner known as a superpartner. SUSY can explain some of the mysteries left by the Standard Model, such as why gravity is weaker than other forces, the existence of the Higgs boson, and it even provides a potential explanation for the source of dark matter [26].

CHAPTER 4

Analysis Objective

The primary objective of this analysis is to explore unmeasured semileptonic decay modes of the B meson, specifically $B^- \to D^0\eta\ell^-\bar{\nu}$ and $B \to D^{*0}\eta\ell^-\bar{\nu}$; these decay modes have never been measured due to their suffering from a very large combinatorial background. $\Upsilon(4S)$ candidates are reconstructed from two semileptonic B decay candidates, where each B decay candidate can be in any of the reconstructed semileptonic decay modes, including $D^{(*)}\ell\nu$, $D^{(*)}\pi\ell\nu$, and $D^{(*)}\eta\ell\nu$. For this study, in each event B^-_{sig} is reconstructed as $D^{(*)0}\eta l^-\bar{\nu}$ (signal) and B^+_{tag} as $\bar{D}^{(*)0}l^+\nu$ (tagging). This chapter details the methodologies used to separate signal from background, with a focus on distinguishing between events with a real eta meson (signal) and combinatorial background, in addition to subtracting peaking background from signal events. Peaking background refers to events that mimic the signal in mass but arise from different decay processes, while combinatorial background consists of random combinations of particles that form a candidate event but do not represent a true signal decay. In order to model the signal and background distributions in the MC sample, a binned χ^2 fit is employed where the smooth background function will be described by a Legendre polynomial, and the signal peaking component will be described by the Crystal Ball function [29]. From this fit, the estimated number of eta signal events is extracted, which in turn is utilized in Chapter 5 to calculate the signal efficiency. This efficiency factor is then used to calculate the branching fraction for the decay mode of interest, $B^- \to D^{(*)0}\eta\ell^-\bar{\nu}$. Additionally, a machine learning model is employed to differentiate between the signal and peaking background. The data utilized in this chapter includes signal modes from the MC signal sample and both peaking and combinatorial backgrounds from the MC generic sample.

4.1 Particle Reconstruction

Event reconstruction involves analyzing the electronic signals captured by a detector to deduce the types of particles that traverse it and their properties. In high energy physics

experiments, direct detection of all particles is not feasible due to the limitations of current detector technologies, the nature of certain particles, and geometrical acceptance. Detectors are typically designed to directly observe a subset of particles that leave distinct signatures. These directly detectable particles include photons, electrons, muons, and charged hadrons (such as pions, kaons, and protons), as well as neutrals that decay into photons (for example, neutral pions and eta mesons). As it is discussed in Chapter 3, each of these particles interacts with the detector material in a way that can be measured and recorded, whether through ionization (charged particles), electromagnetic showers (photons and electrons), hadronic showers or penetration and decay signatures (muons and neutral hadrons). The aim is to trace the origins of the detected particles to their parent particles, often involving complex decay chains. The challenge and skill in event reconstruction lie in using the observed tracks and energy deposits of these detectable particles to infer the presence and properties of short-lived particles or those that rarely interact with the detector material, such as neutrinos.

In studies of B mesons produced at electron-positron colliders, two main methods are used, **tagged** and **untagged** analysis, to reconstruct $\Upsilon(4S)$ events that include the B-meson decay channel of interest.

4.1.1 Tagged and Untagged Analysis

In **untagged** analyses, the focus is on identifying the decay products of just one of the B mesons (B_{sig}) from the $\Upsilon(4S)$ decay, and the other B meson (B_{tag}) is not specifically identified directly. Instead, all the other particles detected in the event are assumed to come from the decay of the second B meson. To ensure that events under examination truly originate from B meson decays, careful selection criteria are applied, given the fact that neutrinos are not detected. Any missing energy and momentum in the event are assumed to be attributable to neutrinos from the B_{sig} decay. In the context of **tagged** analyses, the decay process of $\Upsilon(4S)$ into two daughter B mesons is examined. One of these mesons is designated as the signal B meson (B_{sig}), and the other serves as the tagging B meson (B_{tag}). The analysis entails the detailed reconstruction of both mesons' decay modes, providing a complete view of the $\Upsilon(4S)$ decay dynamics. The reconstruction of B_{tag} employs a variety of exclusive decay modes, categorized into hadronic and semileptonic types, which was explained in Section 2.4. For the analysis conducted in this study, both B mesons are reconstructed through semileptonic decay channels. Specifically, B_{sig} decays into $D^{(*)}\eta\ell\nu$ while B_{tag} decays into $D^{(*)}\ell\nu$.

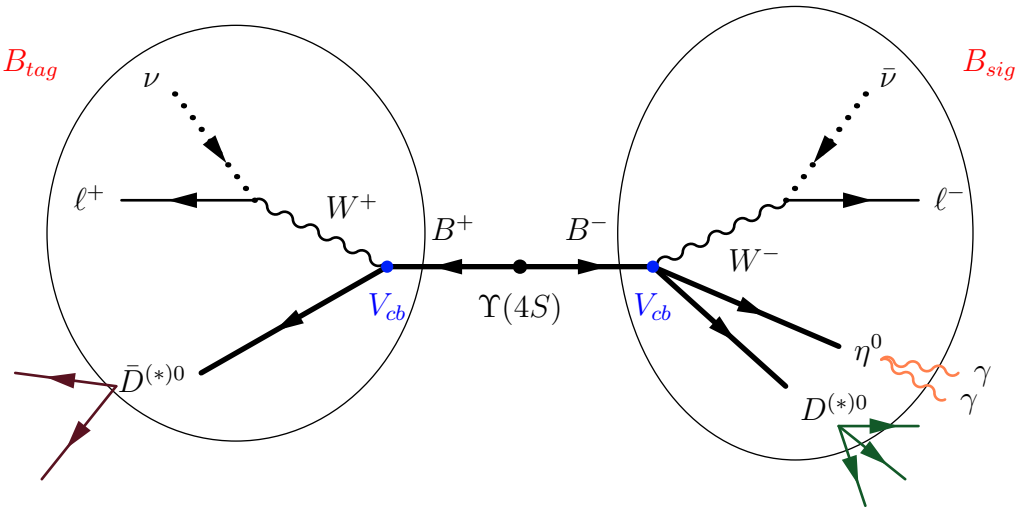

Figure 4.1: **B Meson Tagged Analysis** - The diagram shows two B mesons, B^+ and B^-, originating from a quark-antiquark pair ($\Upsilon(4S)$). B_{sig} represents the signal B meson decay mode of interest, while B_{tag} serves as the tag side, reconstructed to reduce the combinatorial background.

4.1.2 Pre-Selection

The reconstruction process begins with the identification of the decay channel of interest, dictating the specific particles and interactions under investigation. The process then advances by listing and identifying the final-state particles, those directly observed in the detector, using the BASF2 modules. This involves measuring the momentum and position of charged tracks and the energy and position of calorimeter clusters, which provide the essential data inputs for further analysis within the BASF2 framework. In this report, the focus is placed on identifying photons, electrons, muons, charged kaons and pions, and their antiparticles as the final-state components. Following the identification of final-state particles, the next step in the reconstruction process involves combining these particles to analyze intermediate particles, which have decayed into the detected final-state particles or other intermediates. The intermediate particles of interest in this thesis will specifically include the $\pi^0 \to \gamma\gamma$, $\eta \to \gamma\gamma$, $K_s^0 \to \pi^+\pi^-$, $D^{(*)}$, and B mesons, and by combining two B mesons, the $\Upsilon(4S)$ resonance is reconstructed. In the reconstruction process, both final-state particles and intermediate particles are combined to reconstruct each B meson; for clarity and distinction within this report, the first B meson reconstructed is labeled as B0 and the second as B1. It is important to note that this labeling does not imply any prioritization or hierarchy between the two; it merely serves as a method to differentiate the two B mesons reconstructed in the analysis. Building upon the reconstruction of intermediate and final-state particles, it is crucial to employ specific selection criteria for each particle

type to ensure purity and accuracy in the analysis. These selection criteria, applied through conditions such as particle identification scores and spatial acceptance, and kinematic constraints, filter the dataset. This filtration helps in isolating particles that are most likely to have originated from the interactions of interest, thus minimizing background noise and enhancing the signal-to-noise ratio. Below, some of these criteria used in this analysis in the BASF2 framework are explained in detail to provide a clearer understanding of their role in the particle selection process.

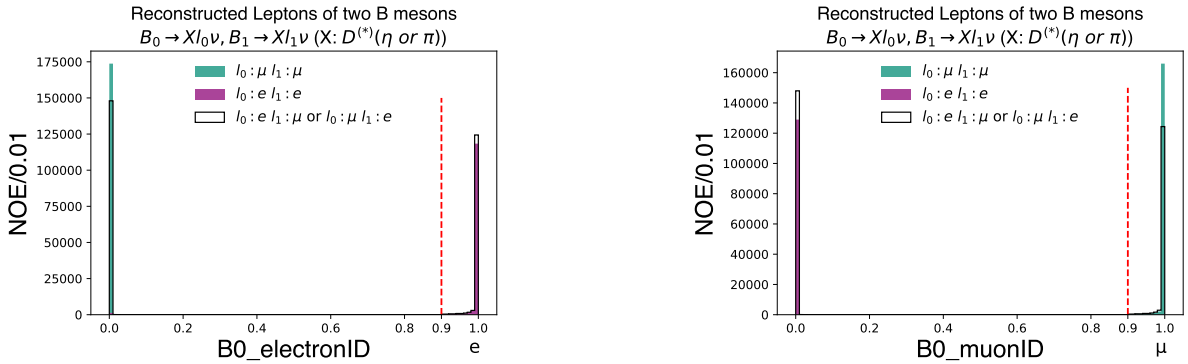

Figure 4.2: **Particle IDentification (PID) for Reconstructed Leptons in B Meson Decays** - The left histogram represents the electron identification (electronID) variable used for lepton discrimination in the BASF2 framework, with a defined cut-off at electronID > 0.9 to separate electrons (above the threshold) from other particles (below the threshold) in the decay products of two B mesons (B0 and B1). Only tracks that have been identified as either e or μ are included in the ntuple as lepton candidates, although some of these candidates are non-lepton particles, such as pions or kaons, that are misidentified as leptons as shown in Figure 4.8a. The x-axis displays the electron or muon ID for leptons originating from B0, while the y-axis quantifies the number of events per bin width. Similarly, a muonID variable (right histogram) applies an equivalent threshold for muon identification. The requirement for the analysis is the reconstruction of at least two leptons, indicating that each B meson decays into a lepton, which can be an electron or a muon, allowing for events where both mesons decay into the same type of lepton or into different types.

(a) **Particle Identification (PID)**: Particle IDentification (PID) is a method that assigns a probability to each detected particle, and indicates the likelihood that it is one of several possible particle types; as Figure 4.2 demonstrates, the lepton will be identified as an electron if the electron ID exceeds 0.9. The PID for an electron, as defined by the formula 4.1, calculates the likelihood of a particle being an electron (L_e) against the summed likelihoods of it being any other particle type in the set. The likelihood is a function dependent on several input parameters, including track momentum, shower energy, and shower shape, among others.

$$\texttt{electronID} = \frac{L_e}{L_e + L_\mu + L_\pi + L_K + L_p + L_d} \tag{4.1}$$

In this formula, L represents the likelihood of a particle being identified as an electron (L_e), muon (L_μ), pion (L_π), kaon (L_K), proton (L_p), or deuteron (L_d).

(b) **Acceptance**: Within the BASF2 framework, there are a series of online cuts known as "acceptance", one notable example being `thetaInCDCAcceptance`. This specific criterion evaluates whether a particle's trajectory falls within the CDC's (section 3.3.2) angular coverage by assessing its polar angle, θ. It returns true if the particle's θ lies between 17 and 150 degrees, indicating that the particle is within the CDC's field of view, and false otherwise; Figure 4.3 shows the cosine of this angle for the lepton (e or μ) reconstructed as the decay product of one of the B mesons (B0). This angle is determined based on the particle's initial momentum, which ensures that only particles with trajectories capable of being tracked and analyzed by the CDC are considered for further analysis.

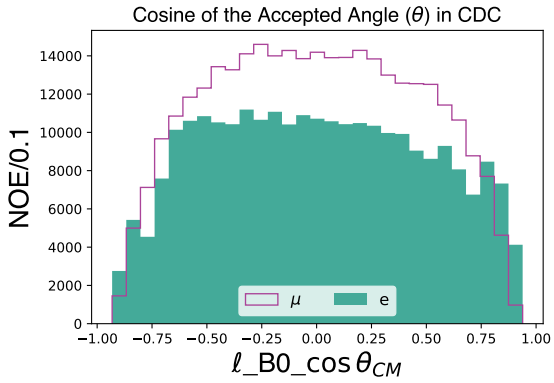

Figure 4.3: **Distribution of $\cos\theta_{CDC}$ for Leptons** - This histogram shows the cosine of the accepted polar angle (θ) in the CDC (section 3.3.2) for electrons and muons. The BASF2 online cut requires that the actual polar angle be within 17 to 150 degrees, although it is the cosine of this angle that is recorded and presented here. The x-axis depicts the cosine of the polar angle for leptons coming from B0, and the y-axis indicates the number of events for each bin width.

(c) **Impact Parameter**: The distance from the Interaction Point (IP), where the e^+e^- collision occurs, to the nearest point on a particle's trajectories is quantified by the vertex parameters `dr` and `dz`, the radial and z-component of this distance respectively. These variables are attributed to charged final-state tracks ($e^\pm, \mu^\pm, \pi^\pm, K^\pm$), and their

values are particularly significant as they enable the discrimination between particles produced in the initial stages of the decay chain and those from subsequent decays, with tracks originating at greater distances from the IP.

(d) **Kinematics**: Kinematic variables such as momentum `p`, energy `E`, and mass `InvM` describe the behavior and properties of particles produced in the collision. Transverse momentum `pt` measures a particle's momentum perpendicular to the beam axis, while momentum in the center-of-mass-system, calculated using `useCMSFrame(variable)` function, assesses a particle's momentum relative to the collision's overall frame. Figure 4.4a and 4.4b illustrate the energy of the higher and lower energy photons reconstructed as the daughters of either η and π^0 coming from B0, and the momentum of the e or μ, the daughter of B0 in the center of mass frame, respectively. In addition to basic kinematics, the variable `dM` represents the difference between the measured mass of a composite particle[1] and its well-established nominal mass[2]; an absolute value of `dM` close to zero indicates a high likelihood that the particle combination is consistent with the hypothesis that it came from the specified parent particle. As an example, Figure 4.4c shows the difference between the reconstructed mass of neutral and charged D or D^* for all reconstructed modes of D meson in this analysis and the nominal $D^{(*)}$ meson masses.

(e) **ECL Cluster**: As particles shower within the ECL (Section 3.3.4), they can excite several crystals due to the energy deposit. The variable `clusterNHits` denotes the total count of crystals affected within a specific cluster, which is an integer corresponding to the crystal count if clusters do not overlap. However, if energy is distributed among adjacent clusters, the resultant sum may be a fractional value.

[1] In case some daughter particles (decay products) may be undetected or missed in the analysis.

[2] The widely accepted and precisely measured mass value of a particle, as determined through numerous experiments and recorded in scientific literature, such as the Particle Data Group (PDG) listings [17].

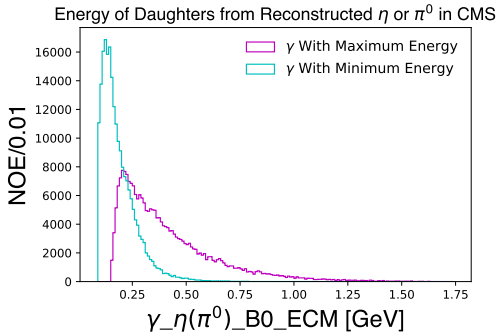

(a) **Photon Energy Distribution** - This plot represents the energy distribution of the photons from the decay of reconstructed η or π^0 in the CMS. The blue histogram indicates the distribution of the photon with the minimum energy, while the other histogram represents the photon with maximum energy in the event. As it is indicated in the plot, there is a threshold applied to the minimum energy of the photon, set to be above 0.09 GeV. The x-axis quantifies the energy of the photons as decay products of either η or π^0 mesons originating from B0 and the y-axis shows the number of events per bin width.

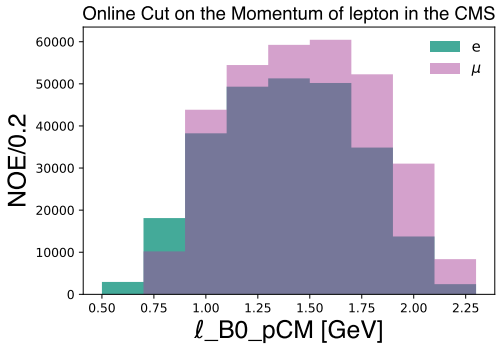

(b) **Momentum of Lepton in the CMS** - The plot visualizes the momentum distribution of leptons (electrons and muons) originating from B0 meson decays in the CMS. The x-axis denotes the lepton's momentum, and the y-axis represents the number of events per bin. The histograms display the online kinematic constraints: the electron's momentum is required to exceed 0.5 GeV, while the muon's momentum must surpass 0.8 GeV within the CMS.

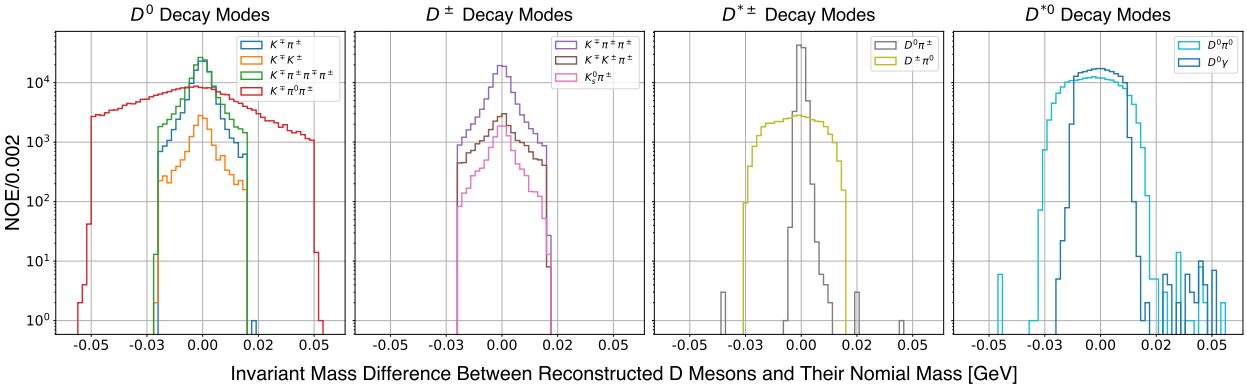

(c) **Differences in Reconstructed vs. Nominal D Meson Masses** - The plot presents the mass difference (dM) between the reconstructed mass of various D meson states ($D^0, D^{\pm}, D^{*\pm}, D^{*0}$) and their nominal mass values. Each graph represents a distinct D meson species, illustrating the various decay channels that have been reconstructed. The histograms showcase that for decay modes not involving a π^0, dM is constrained to be below 0.02 GeV to ensure a tight selection, reflecting the precision of the reconstruction process. However, in decay modes where a π^0 is present, the selection is loosened to allow dM up to 0.05 GeV; π^0 reconstruction is challenging because the detector's energy resolution is typically less precise for photons compared to charged particles.

Figure 4.4: **Key Kinematic Constraints through BASF2 Framework** - Energy, momentum, and mass distribution of decay products.

(f) **Chiprob and Particle Ranking**: In each event, multiple candidates for the $\Upsilon(4S)$ decay may be reconstructed due to the numerous possible combinations of detected particles that can fit the expected decay patterns. This analysis considers a maximum of 9 $\Upsilon(4S)$ candidates per event. The selection of the best candidate often involves ranking these candidates based on certain variables related to their likelihood of representing a true decay. The process starts with vertex fitting, as exemplified by the `vertex.treeFit` function, which performs a global fit to the entire decay chain. It optimizes the decay vertices and particle momenta under the constraints of the decay hypothesis. The fit's quality is quantified using the chi-squared statistic, χ^2, which sums the squared differences between the expectation (e) and the measurement (m), divided by the variance (σ^2) on the expectation [30]. The fitting procedure takes into account the uncertainties and measurement noise, minimizing the χ^2 value, or maximizing the χ^2 probability, to find the best fit to the data.

$$\chi^2 = \sum \frac{(e-m)^2}{\sigma^2}$$

Once the fitting process is complete within the BASF2, the candidates are organized in order of their fit quality using a ranking module. This is accomplished via the `rankByHighest` or `rankByLowest` functions, which depend on whether one seeks to prioritize candidates with higher or lower values of a specified variable, respectively. In this particular analysis, the χ^2 probability is chosen as one of the bases for ranking, and the pre-selection has up to 9 $\Upsilon(4S)$ candidates per event. Figure 4.5 displays the average chi-squared probability for B0 and B1, incorporating all nine $\Upsilon(4S)$ candidates per event.

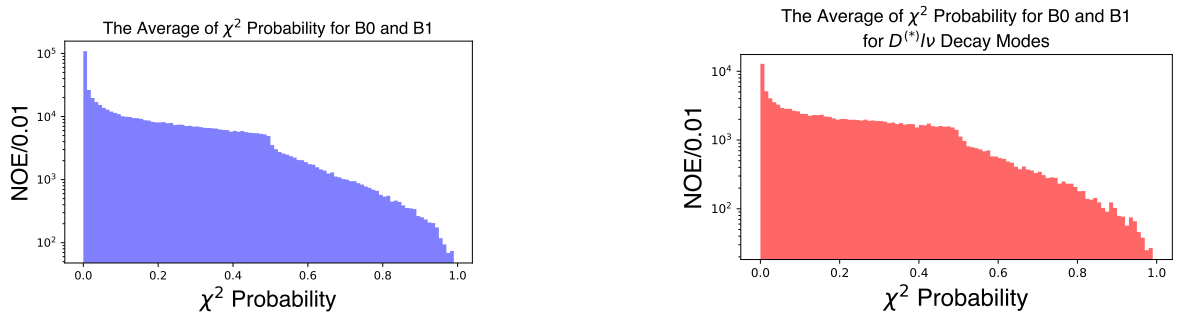

Figure 4.5: **Chi-Squared Probability Distribution per $\Upsilon(4S)$ Candidate** - The left plot illustrates the average chi-squared probability between B0 and B1 in each event, using chi-squared (χ^2) probability, while the right plot demonstrates the average χ^2 probability when at least one of the B mesons is reconstructed as $D^{(*)}\ell\nu$ and their origin has been truth matched. The selection retains 9 best $\Upsilon(4S)$ candidates.

(g) **Rest Of Event (ROE)**: After reconstructing the signal particle list, it becomes essential to examine the particles that are not associated with the signal list. These are referred to as Rest Of Event (ROE) particles. After reconstructing the $\Upsilon(4S)$ resonance, any particles not included in this reconstruction are collectively referred to as the ROE. Some key ROE variables that offer valuable insight include the ROE's total energy and the count of charged particles within the ROE, which are denoted as Eextra_ROE and nROE_Ch, respectively, in the Figure 4.6.

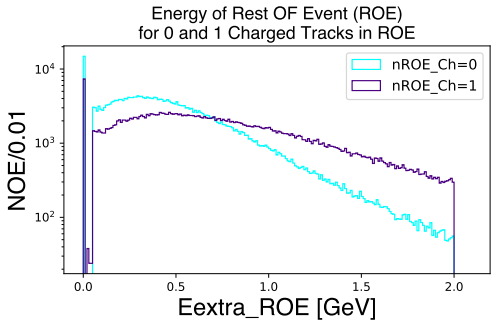

Figure 4.6: **ROE Energy Distribution for Events with Zero and One Charged Track** - This plot depicts the energy distribution of the Rest Of Event (ROE) with a distinction made between events containing zero and one charged particles within the ROE. The x-axis, labeled Eextra_ROE, ranges from 0 to 2 GeV. In fact, the Eextra_ROE represents the total energy of all particles in the Rest Of Event. The histograms show how the ROE energy is spread across this range, with the blue histogram representing events with one charged track (nROE_Ch = 1) and the purple histogram representing events with no charged tracks (nROE_Ch = 0) in the ROE.

In constructing the ROE, it is essential to recognize that not all particles outside the signal particle list are automatically classified as ROE. Instead, a selection process determines what constitutes an ROE particle, which is governed by specific acceptance cuts: energy threshold, angle constraints, or other parameters derived from reconstructed quantities. These acceptance cuts are implemented through ROE masks, which serve to filter the particle content and ensure that the ROE consists of particles that meet the established criteria, rather than an inclusion of all non-signal entities.

(h) **Eta and Neutral Pion Mesons Reconstruction**: In this analysis, each event involves selecting two random photons with energies within the range depicted in Figure 4.4a ($E > 90$ MeV), which are then used to reconstruct either an η or a π^0 meson. Shown below is the conservation of the four-momentum of the η or π^0 for this two-body decay system.

$$\begin{aligned} M^2_{\pi^0,\eta} &= ((E_{\gamma_1} + E_{\gamma_2})\ ,\ (\vec{P}_{\gamma_1} + \vec{P}_{\gamma_2}))^2 \quad \text{Because } M_\gamma = 0 \quad \Rightarrow E_\gamma = |\vec{P}_\gamma| \\ M^2_{\pi^0,\eta} &= 2E_{\gamma_1}E_{\gamma_2}(1 - \cos\theta_{\gamma_1,\gamma_2}) \qquad\qquad \text{And } -1 \leq \cos\theta_{\gamma_1,\gamma_2} \leq 1 \end{aligned}$$

$$\text{Therefore, } M^2_{\pi^0,\eta} \in [0, 4E_{\gamma_1}E_{\gamma_2}] \tag{4.2}$$

The formula illustrates that since the cosine of the angle between the two photons can assume any value between -1 and 1, the system's invariant mass squared can range from zero to four times the product of the energies of each photon. Depending on the event, the two randomly selected photons can have closely matched or significantly different energies. Consequently, the resulting invariant mass ($M_{\pi^0,\eta}$) for each pair can span various subranges within the overall range in formula 4.2. The aggregation of subranges from different events, corresponding to individual photon pairs, creates the overall distribution profile for the reconstructed masses of η or π^0 mesons. Figure 4.7 displays the mass distribution of reconstructed photon pairs, with peaks corresponding to the π^0 and η mass regions.

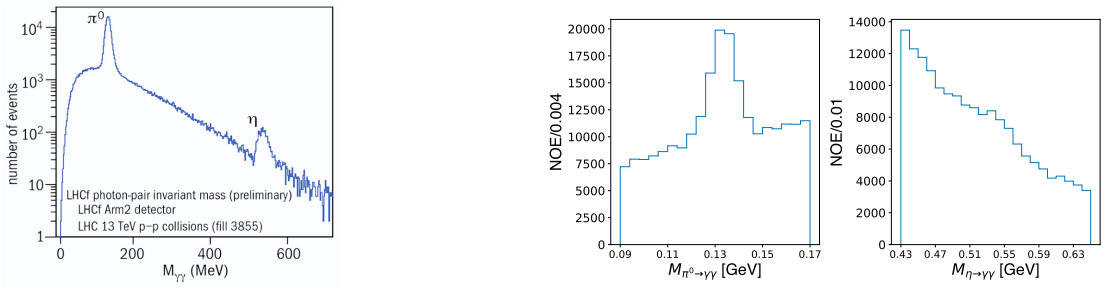

(a) From proton-proton collisions [31] (b) From Belle II MC Generic Sample

Figure 4.7: **Reconstructed Invariant Mass Distribution of Photon Pairs** - Mass distribution of reconstructing photon pairs showing peaks corresponding to π^0 and η mesons; Plot (b) incorporates additional online cuts on the π^0 and η mass range via the BASF2 framework to enhance background suppression.

4.2 Data Selection

After defining all the necessary online cuts through the BASF2 for the purpose of data reconstruction, the subsequent step involves running computational jobs that can be executed on either MC **signal**[3] or **generic**[4] samples for signal and background events, respectively. The choice between signal and generic samples depends on the specific objectives of the analysis.

Generic Sample is a broad, all-encompassing simulation that aims to replicate the full spectrum of $B\bar{B}$ processes that can occur within the experiment. It includes various decay channels, background processes, and interactions, making it a comprehensive dataset that represents a wide array of $B\bar{B}$ events that the experiment could detect.

Signal Sample is specifically tailored to fill in the gaps in our understanding or simulation coverage of certain physics processes. This means it focuses on particular decay modes or interactions that are not well represented in the more comprehensive datasets like generic samples. In fact, the four-body phase space model in the generic sample is unsuitable for signal modes ($B^- \to D^{(*)0}\eta\ell^-\bar{\nu}$) primarily because it assumes a uniform distribution of decay products across the available kinematic space, neglecting crucial physical constraints such as resonance structures and conservation laws. As a result, the model treats every configuration of the decay products – the position and momenta of $D^{(*)}$, η, ℓ, and ν – as having the same likelihood of occurring. This model fails to

[3]It is referred to as gap sample internally within the semileptonic B meson group in Belle II

[4]All the plots illustrating the reconstruction criteria in section 4.1 and 4.2 are generated using the generic dataset.

capture the complex interactions and correlated behaviors between particles, such as specific angular momentum and energy distributions, and therefore oversimplifications lead to inaccurate simulations of the decay dynamics, which will be shown in Results Chapter 5 in Table 5.1.

In this analysis, the signal mode focuses on the decays of $D^{**}\ell\nu$ generated using the LLSW model [32]. Here, D^{**} represents excited states of the charm meson, specifically either D_1' or D_0^*, which then are forced to decay to $D^{(*)}\eta$.

Table 4.1 is a summarized overview of each sample, detailing their respective cross-sections (σ), the number of $B\bar{B}$ pairs generated, and the corresponding integrated luminosity $\mathcal{L}$. Luminosity and cross-section in particle physics quantify the production rate of events in a collider experiment. The cross-section measures the likelihood of a specific process occurring, which is intrinsic to the process itself and expressed in units of barns, with 1 barn equivalent to 10^{-28} square meters. The integrated luminosity relates to the total number of potential collisions over a given period and is a measure of the dataset's size. These quantities are related by the formula 4.3.

$$N(B\bar{B}) = \sigma(B\bar{B}) \,.\, \mathcal{L} \tag{4.3}$$

Table 4.1: **Quantitative Summary of Generic and Signal Sample Datasets** - This table provides a comparative summary of the generic and signal datasets used in the analysis, detailing the number of simulated $B\bar{B}$ pairs, the cross-sections for $B\bar{B}$ production, and the integrated luminosities. The signal sample specifically targets B meson decays to $D^{**}\ell\nu$, with D^{**} denoting either a D_0^* or a D_1' meson, which then decay into $D\eta$ or $D^*\eta$, respectively.

Sample	Simulated sample size		
	$N(B^+B^-)$	$\sigma(B^+B^-)\cdot BF$	$\mathcal{L}$
Generic			
	5.08×10^8	54×10^7 ab	0.9 ab^{-1}
Signal Sample[5]			
$B^- \to [D_0^{*0} \to D^0\eta]\ell^-\bar{\nu}$	8.00×10^6	43×10^5 ab	1.8 ab^{-1}
$B^- \to [D_1'^0 \to D^{*0}\eta]\ell^-\bar{\nu}$	8.00×10^6	43×10^5 ab	1.8 ab^{-1}

Where N represents the number of events produced, for the signal sample, one B decays to specific modes ($D_1'\ell\nu$ and $D_0^*\ell\nu$), which decay into $D\eta$ or $D^*\eta$; the other B decays generically. As a result the cross-section calculated for this sample only reflects these targeted decay modes and not the complete range of possible decays of B meson. Therefore, the $\sigma_{-}\ B\bar{B}$ has been adjusted by multiplying it with the MC estimated branching fraction for the decay mode of $B^- \rightarrow D^{(*)0}\eta\ell^-\bar{\nu}$, where ℓ includes both electrons and muons, with a value of 2.01×10^{-3}.

4.2.1 Signal and Background Samples

The analysis started by reviewing general information about the dataset and establishing some offline cuts[6], the specifics of which will be detailed in the following sections. These cuts include selecting the best candidate from multiple event candidates, applying an energy cut to the Rest Of Event (ROE), and restricting the analysis to only charged modes of B mesons. This initial phase utilized half of the generic dataset, selected to approximate the size of the current Belle II data sample, with the integrated luminosity of 456.10 fb^{-1} [33]. Subsequently, the focus narrowed to the mode of interest, where one B meson is reconstructed as $D^{(*)0}\eta\ell^-\bar{\nu}$ and the other as $\bar{D}^{(*)0}\ell^+\nu$. In this phase, signal events were sourced from the signal sample, while the background events were drawn from the generic sample. To ensure the reliability of the findings, the combined MC dataset of signal and generic samples was divided into two equal parts, where each half corresponds to an effective luminosity of 470.78 fb^{-1}. One-half of the dataset will be utilized as an MC dataset for conducting the analysis, while the other half will serve as the pseudo-data set to validate and cross-check the results.

4.2.2 Best Candidate Selection

This is a candidate selection strategy designed to identify and select the most suitable $\Upsilon(4S)$ candidate in each event. Initially, 'candidate0' is considered the best out of 9 $\Upsilon(4S)$ candidates as shown in Figure 4.5 due to preliminary evaluations. However, after applying specific event selection criteria, 'candidate0' might be excluded in some cases, e.g. if it was reconstructed in a different decay mode than the signal plus tag mode. Consequently, the strategy adjusts by selecting the first available signal candidate in the event post-criteria, ensuring that the best possible signal candidate is chosen based on the revised conditions.

[5]The number of $B\bar{B}$ pairs generated in each signal sample is 10^7, of which 80% are produced with beam background included and used in this analysis.

[6]The term "offline cut" refers to the selection criteria applied in the analysis after the initial pre-selection stage on BASF2

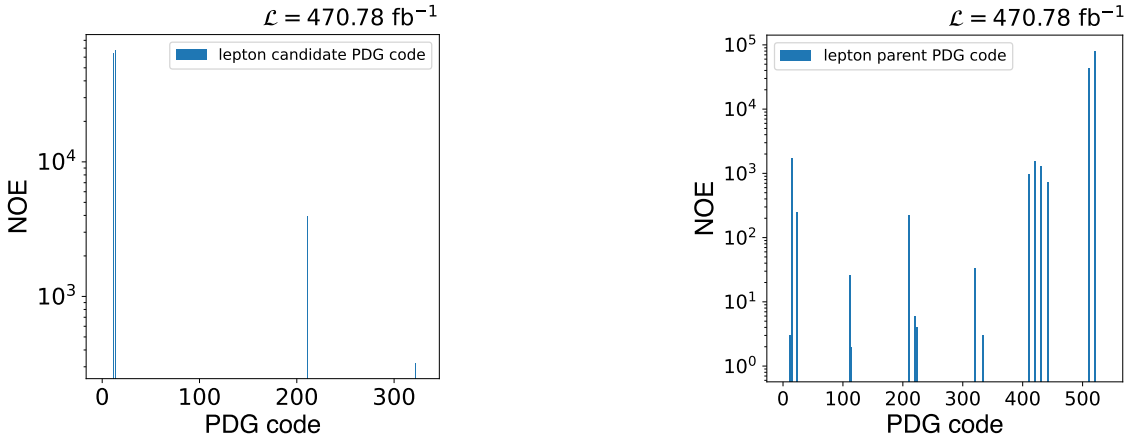

(a) True PDG Codes of Leptons Reconstructed in B Meson Decays

(b) Origins of Reconstructed Leptons: Verification of Parent PDG Codes

Figure 4.8: **Validation of Lepton Identification and Origin in B Meson Decays** - These plots validate lepton identification and origin in B Meson decays. The left plot displays the PDG codes for reconstructed leptons, with codes 11 and 13 confirming identified electrons and muons, respectively; where the presence of codes other than 11 and 13 suggests alternative particles like pions or kaons. The right plot reveals the parent of reconstructed leptons, primarily identifying charged and neutral B mesons as the source with the PDG codes of 521 and 511 respectively, with a few cases of other particles like D mesons including D^+ (411), D^0 (421), and D_s^+ (431). The plots indicate over 95% accuracy in lepton identification and correct decay attribution

4.2.3 Reconstructed and MC_Truth Variables

After particle reconstruction, data stored in an n-tuple contain "reconstructed" and "mc_truth" variables. "reconstructed" variables are derived from Monte Carlo simulations that mimic expected experimental outcomes. "mc_truth" variables represent the true conditions of these simulations before considering the effects of the detector or experimental environment. These variables help in comparing and calibrating real experimental data against theoretical models. Mc_truth variables can validate particle identification, and enable confirming whether a reconstructed particle is indeed the particle it is identified as, and in the case of decay products, whether they genuinely come from the expected parent particle. For instance, the provided plots in Figure 4.8 display the PDG codes for leptons identified in an event. The left plot indicates the PDG codes for direct lepton candidates, confirming the identification of true leptons (either muons or electrons). The right plot shows the origin of these leptons, specifically if they are direct decay products of B mesons or other particles (e.g. charged and neutral D or strange D mesons). From these plots, it can be inferred that lepton identifi-

cation is achieved effectively: only about 3% of leptons are misidentified (fake), and merely 5% are incorrectly associated as decay products of B mesons.

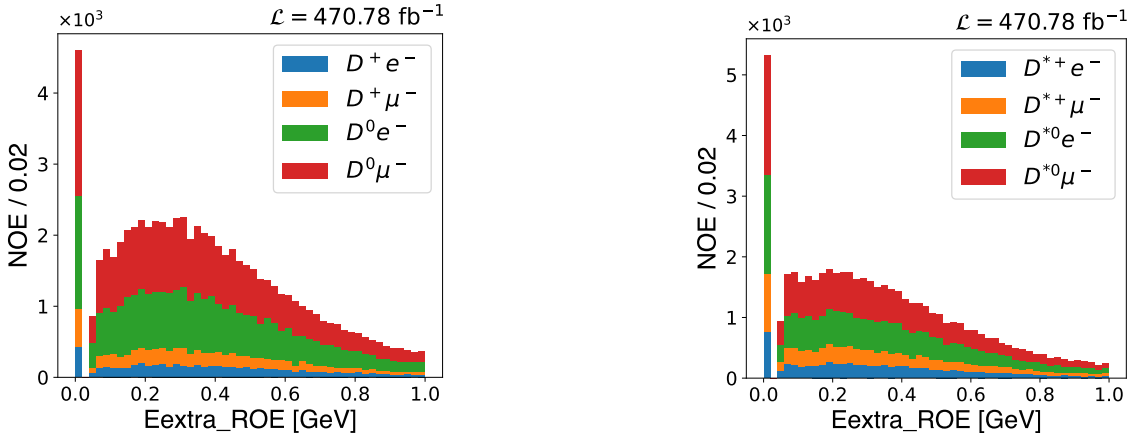

(a) ROE Energy Spectrum for $D\ell\nu$

(b) ROE Energy Spectrum for $D^*\ell\nu$

Figure 4.9: **Comparative Energy Distribution of the Rest Of Event in D and D^* Semileptonic B Decays** - The plots represent the energy distributions of the Rest Of Event (ROE) for semileptonic B mesons when at least one of them is reconstructed as D or D^* mesons, and either an electron or a muon with zero charged tracks in ROE. In (a), the ROE energy for events where at least one B meson was reconstructed as $D\ell\nu$ is plotted, while (b) focuses on the events where at least one of the B mesons is reconstructed as $D^*\ell\nu$. The sharp peak at zero indicates efficient event reconstruction with minimal missing energy, while events with ROE energy above 1 GeV are filtered out. The slight difference in the mean energy between the two plots can be attributed to the occasional missing soft pion in the D^* reconstructions, contributing additional energy to the ROE.

4.2.4 Rest OF Event Cut

As discussed in part (g) in Section 4.1.2, the ROE contains all particles that are not captured in the primary event reconstruction. Ideally, the energy of the ROE, denoted as Eextra_ROE, should be zero, which is supported by Figure 4.9 where most events indeed show Eextra_ROE at zero. This figure also illustrates that events with Eextra_ROE exceeding 1 GeV are excluded from further analysis. Additionally, another cut implemented is the exclusion of charged particles from the ROE.

The plots further differentiate the modes of B meson decay into $D\ell\nu$ (Figure 4.9a) and $D^*\ell\nu$ (Figure 4.9b), where ℓ represents e or μ. In the event, the other B meson can decay into any mode specified in the steering file. A comparison of these plots reveals that the ROE tends to have more energy in (a), where the B meson reconstructed as $D\ell\nu$, averaging 0.37 GeV, as opposed to (b) with the mean of 0.34 GeV. This discrepancy is attributed to

events where a soft pion (π^0) is missed, leading to a D meson being reconstructed instead of a D^*, thus contributing extra energy to the ROE. As a result, this analysis aims to include events where the transition π^0 is missed; hence, the D and D^* mesons are combined in the selection to account for this effect.

4.2.5 Selection of Charged B Meson Decays

In the reconstruction process, each $\Upsilon(4S)$ meson may be categorized into five different B mesons pair modes: B^-B^+, $\bar{B}^0B^0$, B^0B^0, B^-B^0, and $B^-\bar{B}^0$. Using the true decay modes variable (e.g. `B0Mode`) from the ntuple, Figure 4.10 demonstrates the proportion of events that were genuinely produced as either charged or mixed pairs.

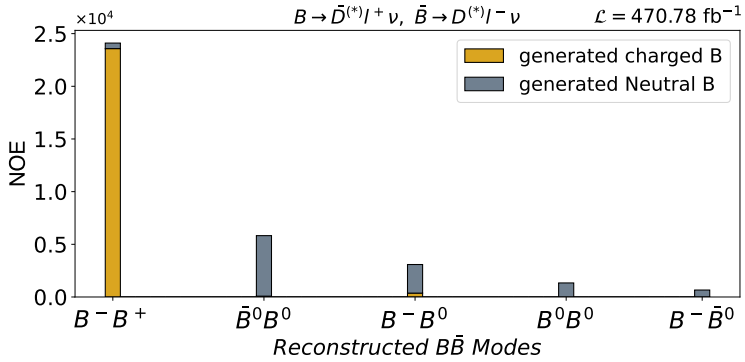

Figure 4.10: **Generated B Decay Modes for Each B Charge and Each $\Upsilon(4S)$ Reconstructed Mode** - The bar chart illustrates the proportions of generated charged and neutral B meson pairs within events where both B mesons are reconstructed as $D^{(*)}\ell\nu$.

Figure 4.10 reveals that events where same-sign leptons are assigned to both B mesons including B^0B^0 and $B^-\bar{B}^0$ – when both leptons are either negative or positive – are considerably rare, compared to B^-B^0 state. A detailed examination of the generated modes for these events, where both B mesons decay to $D^{(*)}\ell\nu$, identified the underlying issue. For charged B mesons, the dataset contains no events reconstructed as $D^{(*)+}\ell^-\bar{\nu}$ in the top plot of Figure 4.11a. Charged B mesons should decay to either D^0 or D^{*0}, where D^{*0} decays into a D^0 with either a π^0 or a γ. Missing a π^0 or a γ results in a D^0 being reconstructed by mistake in place of D^{*0}. The frequency of such misreconstructions – an undetected π^0 or a γ leads to a D^0 misidentified as D^{*0} – is depicted in the bottom part of Figure 4.11a. Conversely, for mixed B meson pairs that decay to $D^{(*)+}\ell^-\bar{\nu}$, a D^{*+} might decay to $D^0\pi^+$ or $D^+\pi^0$. If the π^+ is not detected, a D^0 is mistakenly reconstructed, hence the B^-B^0 state results when a $\bar{B}^0$ is incorrectly identified as a B^-. This misidentification is shown in the

bottom plot of Figure 4.11b, where the misrecontruction of B^- instead of the actual $\bar{B}^0$ accounts for the presence of B^-B^0 events in the data.

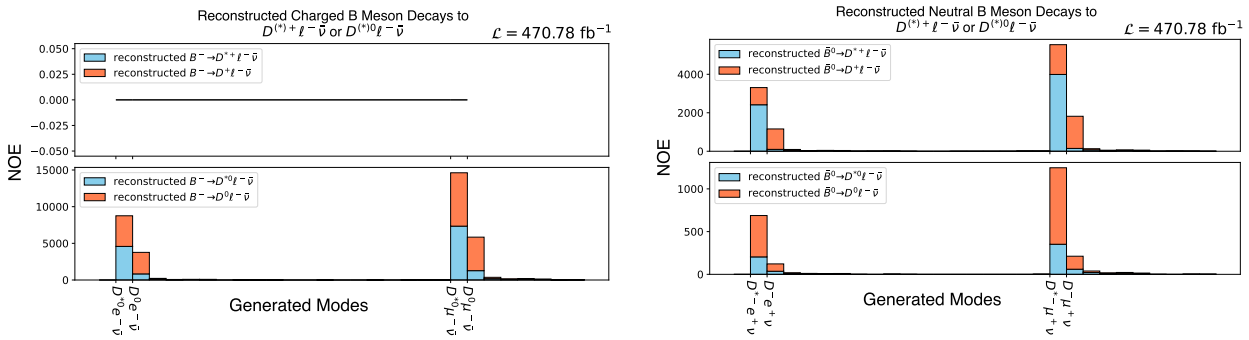

(a) Charged (b) Mixed

Figure 4.11: **True Decay Origin for Decays Reconstructed as $D\ell\nu$ or $D^*\ell\nu$** - Plot (a) focuses on charged B mesons, highlighting the absence of misidentified $D^{(*)+}\ell^-\bar{\nu}$ decays, and plot (b) detailing mixed B mesons, where the missing π^+ leads to B^-B^0 misclassification. The diagonal plots quantify the frequency of inaccuracies in the reconstruction of $D^{(*)+}$ in mixed modes and $D^{(*)0}$ in charged mode. The x-axis of the plots categorizes the events by their generated decay modes, while the y-axis represents the number of events.

Given the clearer signal and larger volume of reconstructed charged B mesons, this mode has been selected for deeper analysis to investigate the signal mode of interest ($B^- \to D^{(*)0}\eta\ell^-\bar{\nu}$).

4.3 Signal and Background Separation

After the selection of charged B meson events with the reconstruction of one as $B^- \to D^{(*)0}\eta\ell^-\bar{\nu}$ and the other as $B^+ \to \bar{D}^{(*)0}\ell^+\nu$, or vice versa, the analysis advances to the next step of signal-background separation. The plot 4.12 illustrates the invariant mass distribution of photon pairs, with a peak around 0.5 GeV, corresponding to the expected invariant mass of the η meson. There are two components in the plot 4.12 with distinct shapes in the MC gamma-gamma mass ($M_{\eta\to\gamma\gamma}$): a peaking component around the eta meson mass and a smoothly varying combinatorial component; the peaking component includes both signal and peaking background. For further analysis, the peaking background and the pure signal will be combined and collectively referred to as the "eta signal". The truth-matching process for signal and background is detailed below.

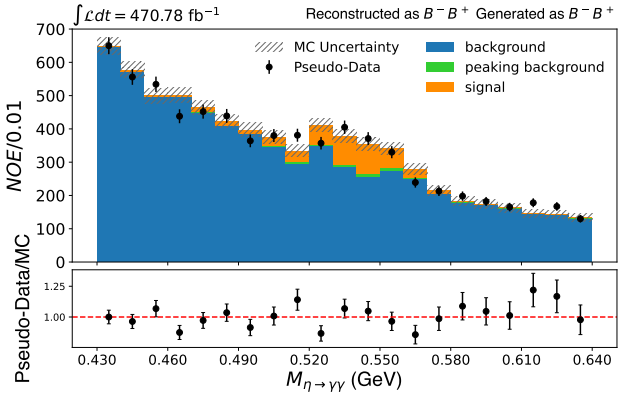

Figure 4.12: **Photon Pairs Mass Spectrum: Separated Signal and Background with Pseudo-Data Overlay** - This plot displays the invariant mass distribution for photon pairs reconstructed as an η meson. The blue area represents the MC simulated combinatorial background with 6653 events, the green area shows the peaking background with 43 events, and the orange area indicates the pure signal with 453 events. The black points represent the pseudo-data and the hatched area covers the MC statistical uncertainty, calculated as the square root of the number of events in each bin; the pseudo-data is the randomly selected half of the dataset from which the MC dataset was picked. The lower panel presents the ratio of pseudo-data to the MC simulation.

- **Signal**: The signal is identified in events where the B meson, reconstructed as the $D^{(*)}\eta\ell\nu$ mode, matches the actual generation of this decay mode, and the η meson, reconstructed from a pair of photons, truly decays into those two photons

- **Peaking Background**: The peaking background in this analysis arises in scenarios where the B meson, reconstructed as $D^{(*)0}\eta\ell^-\bar{\nu}$, is generated as $B^- \to D^{(*)0}D_s^-$ with the D_s subsequently decaying into $\eta\ell\nu$. This specific decay chain mimics the signal due to the identical final states, thereby contributing to the peaking background in the invariant mass distribution of the photon pairs.

- **Combinatorial Background**: The combinatorial background encompasses all events that do not fit into the signal or peaking background categories. Notably, approximately 40% of these combinatorial background events are instances where the B meson, reconstructed as $D^{(*)}\eta\ell\nu$, was actually generated as $D^{(*)}\ell\nu$. Additionally, around 4% of the combinatorial background is attributed to events where the B mesons were generated as neutral $B\bar{B}$ pairs rather than as charged B meson pairs.

The MC sample used in this analysis is created by replacing the signal from the generic MC with the appropriately weighted events from the signal sample. The signal sample contained

1733 signal events, with an integrated luminosity of 1842.64 fb^{-1}, and the generic sample had 590 signal events at 941.56 fb^{-1}. The next step involved replacing the signal events in the generic sample with those from the signal sample scaled by a factor from equation 4.4. This adjusted dataset was then divided equally to form the MC dataset for analysis and the pseudo-data for validation, each with an integrated luminosity of 470.78 fb^{-1}.

$$\text{scale-factor} = \frac{\mathcal{L}^{\text{Background-sample}}}{\mathcal{L}^{\text{signal-sample}}} \tag{4.4}$$

The next step is fitting appropriate functions to the MC dataset; this is started by combining the pure signal events and peaking background to form a unified eta signal and treating the combinatorial background as the sole background component.

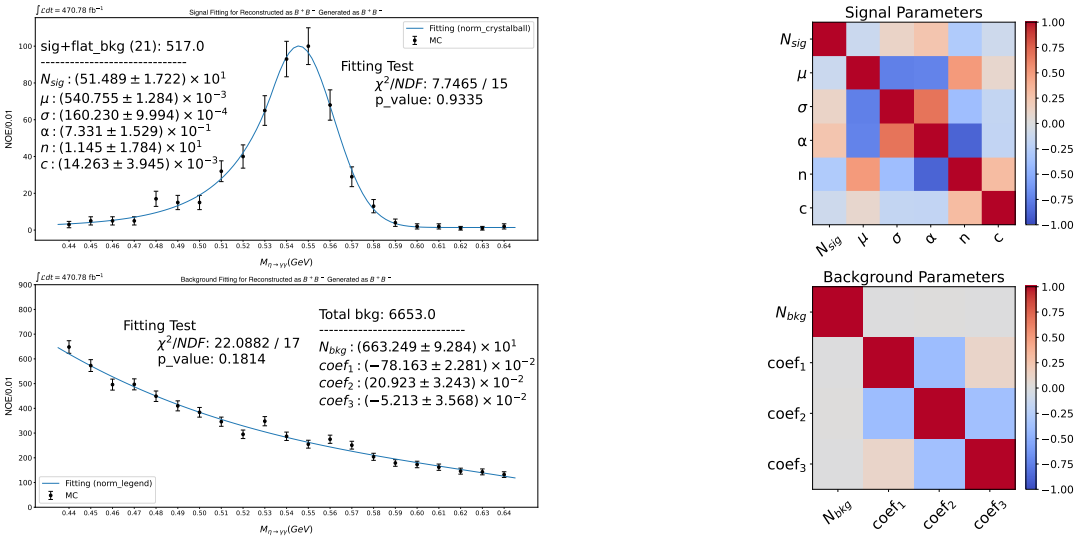

(a) Signal and Background Fits to $M_{\gamma\gamma}$

(b) Correlation Matrix

Figure 4.13: **Separate Fitting Results and Correlation Analysis for Signal and Background for $M_{\gamma\gamma}$** - (a) The top plot details the Crystal Ball function fit the eta signal (pure signal plus peaking background) combined with a flat background, and the bottom plot presents the fit of the first four Legendre polynomials to the combinatorial background. Both plots display the optimized fitting parameters along with their uncertainties. The goodness of each fit has been evaluated using the chi-squared (χ^2) and the p-value. With the chi-squared values close to the degrees of freedom (15 for the eta signal and 17 for the background) and p-value above 5%, these results indicate that the models effectively capture the underlying distributions. (b) The two plots display the correlation matrices between the parameters for both signal and background fits.

4.3.1 Fitting To MC

In the fitting step, the initial phase requires fitting the eta signal and combinatorial background functions independently to their respective distributions (Figure 4.13). Subsequently, a combined function, which includes both the eta signal and combinatorial background functions with some parameters fixed, is fitted simultaneously to the eta signal plus combinatorial background (Figure 4.14). This combined fit is first applied to the MC data to calculate the signal efficiency and then to the pseudo-data to determine the MC branching fraction of the mode of interest ($D^{(*)0}\eta\ell^-\bar{\nu}$).

✦ **Combinatorial Background**

For the combinatorial background function, one of the orthogonal polynomials, the normalized Legendre polynomials, is selected. Orthogonality means that the integral of the product of any two different polynomials over their defined interval is zero. This property ensures that each polynomial contributes independently to the model. As a result, when these polynomials are used as basis functions in a fit, each one adjusts to specific features of the data without interference from the others. The correlation matrix presented in Figure 4.13b demonstrates the low covariance between background parameters. The Legendre polynomials are orthogonal over the interval from -1 to 1. However since the mass range of the reconstructed photons pair is between 0.44 and 0.64 GeV, it is necessary to map each point of the original range to a point between -1 and 1. This mapping is accomplished using the transformation detailed in equation 4.5.

$$x_{\text{mapped}} = -1 + \frac{2(x - x_{\text{min}})}{x_{\text{max}} - x_{\text{min}}} \tag{4.5}$$

The variable x represents a point within the mass range, and x_{mapped} is the corresponding point transformed between -1 and 1, with x_{max} and x_{min} denoting the maximum and the minimum of the original mass range, respectively. Considering the range mapping in the normalization factor, the first four Legendre polynomials are utilized, with each assigned a coefficient. These coefficients are then multiplied by the respective polynomial, and the fit aims to determine the optimal values for each coefficient and the normalization constant N_{bkg}, which provides an estimate of the total number of background events.

$$f_{\text{bkg}}(x, 1, \text{coef}_1, \text{coef}_2, \text{coef}_3) = \frac{N_{bkg}}{N} \cdot (1 + \text{coef}_1 \cdot x + \frac{\text{coef}_2}{2} \cdot (3x^2 - 1) + \frac{\text{coef}_3}{2} \cdot (5x^3 - 3x)) \tag{4.6}$$

where

$$N = 2m \qquad \text{and} \qquad m = \frac{x_{\max} - x_{\min}}{2} \tag{4.7}$$

In equation 4.7, the term m arises due to the range mapping, which is reflected in the normalization factor (N).

✦ **Eta Signal (signal + peaking background)**

The chosen function for the eta signal, including both pure signal and peaking background, is a combination of the normalized crystal Ball function and a flat background ($c = 21$), which is depicted below.

$$f_{\text{sig}}(x;\mu,\sigma,\alpha,n,c) = \frac{N_{\text{sig}}}{N} \cdot \begin{cases} \exp\left(-\frac{(x-\mu)^2}{2\sigma^2}\right) + c, & \text{for } \frac{x-\mu}{\sigma} > -\alpha \\ A \cdot (B - \frac{x-\mu}{\sigma})^{-n} + c, & \text{for } \frac{x-\mu}{\sigma} \leq -\alpha \end{cases} \tag{4.8}$$

where

$$\begin{aligned} A &= \left(\frac{n}{|\alpha|}\right)^n \cdot \exp\left(-\frac{|\alpha|^2}{2}\right), \\ B &= \frac{n}{|\alpha|} - |\alpha|, \\ N &= \sigma(C + D + 2c) \cdot m, \\ m &= \frac{x_{\max} - x_{\min}}{2}, \\ C &= \frac{n}{|\alpha|} \cdot \frac{1}{n-1} \cdot \exp\left(-\frac{|\alpha|^2}{2}\right), \\ D &= \frac{\sqrt{\pi}}{2}\left(1 + \operatorname{erf}\left(\frac{|\alpha|}{\sqrt{2}}\right)\right), \qquad \operatorname{erf} z = \frac{2}{\sqrt{\pi}} \int_0^z e^{-t^2}\, dt. \end{aligned}$$

The parameters used to determine their optimal values include N_{sig}, which provides an estimate of the number of eta signal events, as well as μ, σ, α, n, and c. The inclusion of a flat background is used because, in the same range as the combinatorial background, the eta signal distribution shows some bins with zero events. This situation leads to an infinite chi-squared (χ^2) value during the eta signal fitting process. To resolve it, a flat background is introduced to add one event to each histogram bin, effectively adding a total of 21 events – the number of bins – to the overall eta signal count, and a 'c' term is incorporated into the eta signal model to account for these added events. The details of the fitting test, including the chi-squared statistic and p-value, will be discussed later in this section.

✦ **Eta Signal** (signal + peaking background) **plus Background** (combinatorial background)

In the combined fitting process for both eta signal and combinatorial background, all eta signal and combinatorial background shape parameters are fixed, including the mass of η (μ), mass resolution (σ), and the parameters α and n from the eta signal function, alongside the coefficients from the combinatorial background model. The values are listed in Table 4.2. Also, each normalized function is scaled by a coefficient to estimate the respective numbers of eta signal and combinatorial background events, N_{sig} and N_{bkg}, and then summed together. Therefore, the eta signal and combinatorial background scale factors are optimized through the fitting process.

$$f_{\text{sig + bkg}}(x; N_{\text{sig}}, N_{\text{bkg}}) = N_{\text{sig}} \cdot f_{\text{sig}} + N_{\text{bkg}} \cdot f_{\text{bkg}}$$

Table 4.2: **Fixed Parameters From Eta Signal and Combinatorial Background Fitting** - Tables are display parameters for eta signal and combinatorial background functions, derived from separate fits. These parameters are subsequently fixed and used in a combined fit to both eta signal and combinatorial background MC simultaneously

Signal			
μ	σ	α	n
0.54	0.02	0.73	11.45

Background		
coef_1	coef_2	coef_3
-0.78	0.21	-0.05

The number of eta signal events passed to the fitting function was 496, while the fit predicted 563 ± 61 eta signal events. Similarly, the combinatorial background MC count was 6653, with the fit predicting 6577 ± 97 combinatorial background events. The fitting result indicates a prediction of more eta signal events and fewer combinatorial background events compared to the actual counts. However, the overall sum of events is close to what was expected, differing by only about 9 events. This outcome demonstrates that N_{sig} and N_{bkg} are anti-correlated, as shown in the correlation matrix (Figure 4.14b). As the number of predicted eta signal events increases, the number of combinatorial background events decreases, maintaining an overall balance nearly aligned with the initial MC estimates.

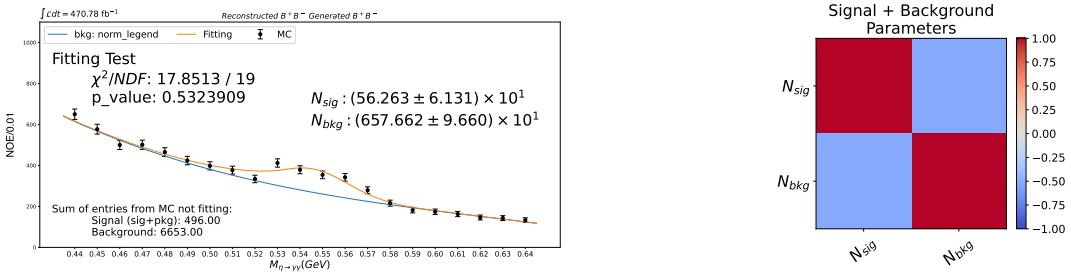

(a) Combined Signal and Background Fit to $M_{\gamma\gamma}$ (b) Correlation Matrix

Figure 4.14: **Combined Fitting and Correlation Analysis of $\gamma\gamma$ Mass Distribution Reconstructed as η for Eta Signal and Combinatorial Background** - (a) The plot depicts the fit result to the photon pair mass spectrum, which includes both eta signal (pure signal + peaking background) and combinatorial background components. The initial MC data provided 496 eta signal events and 6653 combinatorial background events. The plot details optimized fitting parameters and their uncertainties, including the estimated number of eta signal (N_{sig}) and combinatorial background (N_{bkg}) events from the fit. The chi-squared (χ^2) statistic of 18 for the number of degrees of freedom (NDF) 19 and a p-value of 0.5 suggest a well-performing model. (b) This plot shows the correlation matrix for the parameters involved in the fit, highlighting significant anti-correlation between N_{sig} and N_{bkg}. This relationship makes the total number of fitted events remain close to the initial MC estimate, with only a minor difference of 9 events.

Assessing Fit Quality: Methods for Evaluating Fitting Results

✧ Residual

One method to evaluate the consistency of the fitting results with the expected values is by examining the residual plot (Figure 4.15), which illustrates the difference between the expected and predicted data. Vertical error bars quantify the uncertainty of MC number of events ($\sqrt{\text{number of events}}$). The red dashed line marks the point of zero deviation, indicating agreement between the fit and the MC data. Of particular note is that only four points deviate beyond one standard deviation from zero, demonstrating that most observed counts are within one sigma of the predicted values. This close alignment for the majority of data points suggests an acceptable description of the MC data's behavior.

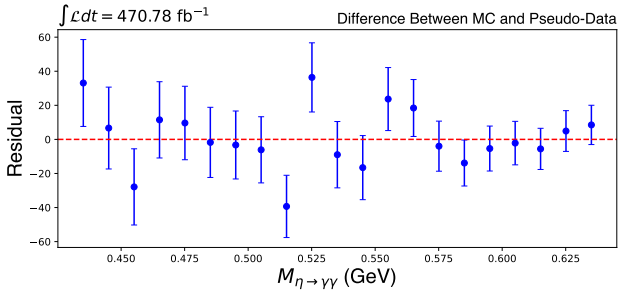

Figure 4.15: **Residual Plot Displaying the Difference Between MC and Pseudo-Data for the η Mass Distribution** - This graph plots the residuals, calculated as the difference in event counts between MC simulations and pseudo-data, against the η mass ($M_{\eta\to\gamma\gamma}$) in GeV. Each point represents the deviation from the expected value, with error bars indicating the propagated uncertainties. The dashed red line at zero represents the ideal scenario where MC and pseudo-data are in perfect agreement. Notably, 6 out of 21 points, or less than 31.8%, deviate from zero by more than one sigma, indicating that the majority of data points align well within their uncertainty range, suggesting a generally good fit between the simulated data and the pseudo-data.

✧ Chi-squared (χ^2) Statistic

The chi-squared (χ^2) statistic is a measure of the discrepancy between observed data and an expected model. It is calculated by summing the squares of the normalized residuals, which are divided by the uncertainty of the MC predictions. It quantifies the extent to which data points deviate from a model, measuring the average magnitude of these deviations. The interpretation of the χ^2 value depends on the degrees of freedom in the dataset, which generally corresponds to the number of observations minus the number of parameters the model has estimated. A good fit yields a χ^2 value close to the Number of Degrees of Freedom (NDF), indicating that the model adequately captures the data's variability. In this case, the χ^2 value is 18 with an NDF of 19, suggesting a well-suited model to the observed sample. A high χ^2 compared to the NDF means the model is wrong or the uncertainties are underestimated. On the other hand, a low χ^2 compared to the NDF might mean the fit line is going through all the error bars suggesting the overestimating uncertainties.

✧ P-value Test

Once the χ^2 value is determined, the p-value can be assessed. The p-value is a probability that indicates how likely it is to observe a χ^2 statistic as extreme as, or more extreme than, the one calculated from the data, assuming that the data were generated as random samples from the model. A high p-value suggests that the observed deviations could be due to

chance alone and it does not give enough evidence to reject the selected model, implying a good fit. Conversely, a low p-value indicates that the observed deviations are unlikely to occur by random variation, suggesting that the model may not adequately explain the data. In practice, a p-value higher than a predefined threshold (often 0.05) is used to infer a statistically satisfactory fit between the model and the observed data. In this analysis, the p-value is 0.53, which exceeds this threshold, indicating a good fit.

4.3.2 Peaking Background Suppression

As explained in the previous section, the peaking background and the signal were initially combined and collectively treated as the eta signal, and a machine learning model has been implemented in order to suppress the peaking background from the signal. The first step in this process is selecting variables capable of providing a discriminant between the true signal and the peaking background.

Discrimination Between Signal and Peaking Background

The signal is defined when the B^- meson is generated as $D^{**0}\ell^-\bar{\nu}$, where D^{**0} represents excited states such as $D_1'^0$ or D_0^{*0}. In these signal events, D^{**0} decays further to D^0 or D^{*0} plus an η meson. Conversely, the peaking background arises when the B^- meson truly decays into a strange D (D_s^-) meson and either D^0 or D^{*0} ($B^- \to D^{(*)0}D_s^{(*)-}$), with the subsequent decay of D_s^- to $\eta\ell^-\bar{\nu}$. Thus, in the case of the signal, the $D^{(*)}$ is a direct daughter of D^{**}, which comes from a 3-body semileptonic B meson decay, whereas in the peaking background, $D^{(*)}$ comes directly from a 2-body B decay. Figure 4.16a illustrates the momentum distribution of $D^{(*)}$ in both peaking background and signal events, where the B^- meson was reconstructed as $D^{(*)0}\eta\ell^-\bar{\nu}$. In the peaking background (green histogram), which involves a two-body decay, the momentum of $D^{(*)0}$ can be predicted using equation 4.9, M is the invariant mass of the particle. According to this formula, the momentum of $D^{(*)}$ in peaking background events should peak around 1.7 GeV.

$$p_{D^{(*)}}^{\text{pkg}} = \frac{\sqrt{[M_B^2 - (M_{D^{(*)}} + M_{D_s})^2]\,[M_B^2 - (M_{D^{(*)}} - M_{D_s})^2]}}{2M_B} \approx 1.7\,\text{GeV} \tag{4.9}$$

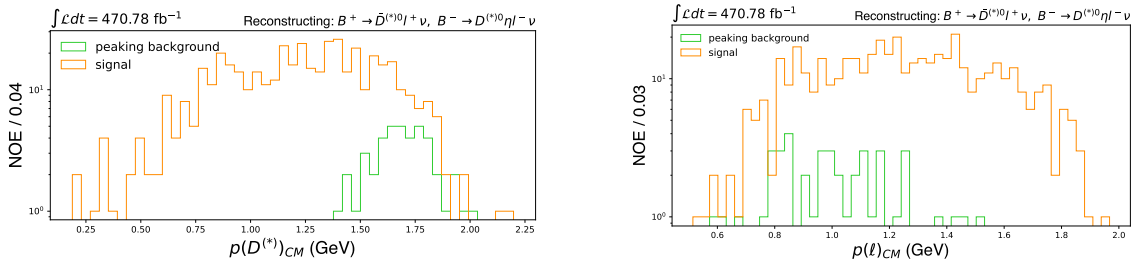

(a) Momentum Distribution of $D^{(*)}$ in Signal and Peaking Background Events

(b) Momentum Distribution of ℓ in Signal and Peaking Background Events

Figure 4.16: **Momentum Distribution for $D^{(*)}$ and Lepton in Signal and Peaking Background Events** - In both plots, one of the B mesons in each event is reconstructed as $D^{(*)}\ell\nu$ and the other as $D^{(*)}\eta\ell\nu$. For peaking background, the B reconstructed as $D^{(*)}\eta\ell\nu$ originates from form a two-body decay $B^- \to D^{(*)0}D_s^{(*)-}$, where D_s decays to $\eta\ell\nu$. In the signal cases, the B is generated as $D^{**}\ell\nu$, with D^{**} being either D_1' or D_0^*. (a) The left plot shows the momentum distribution of $D^{(*)}$ where, in the peaking background, it is derived from the two-body decay momentum in equation 4.9, typically peaking around 1.7 GeV. (b) The right plot details the lepton momentum distribution for the signal candidate and peaking background events.

In the context of lepton momentum in the peaking background and signal events, distinctions also arise based on the decay origins and the spin properties of the hadrons involved. In peaking background events, the lepton is a decay product of the D_s, while in signal events, the lepton originates directly from the B meson decay.

Given the relatively small sample dataset comprising 454 signal events and only 43 peaking background events, four variables, shown in Figure 4.17, have been chosen based on their effectiveness in distinguishing between signal and peaking background. These variables include the invariant masses of combined η and the D meson, and the η and the lepton (ℓ), calculated using Formula 4.10. Additionally, the cosines of the angles between η and D meson, and η and ℓ, computed using Formula 4.11, are utilized. In the context of the signal, the eta and D meson are decay products of the same parent (D^{**}), whereas the eta and the lepton originate from different parents; on the other hand, in the peaking background scenarios, the relationships between these particles are reversed.

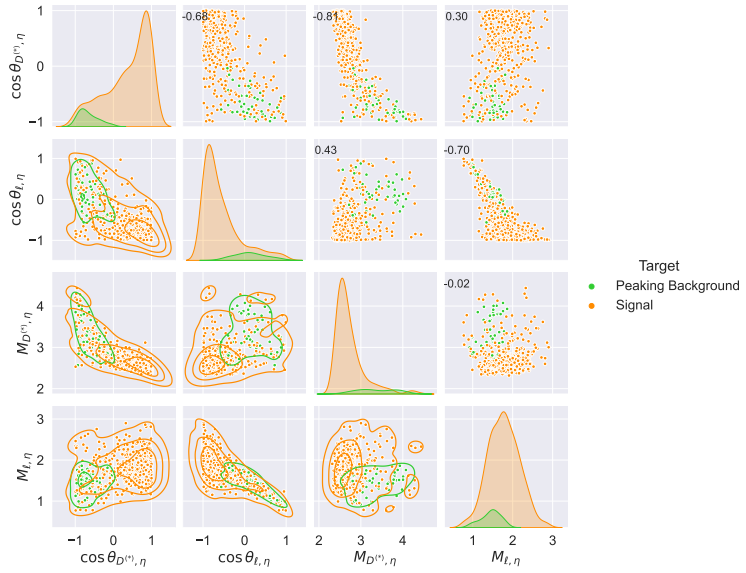

Figure 4.17: **Feature Distributions for Classifier Differentiating Signal and Peaking Background** - This set of plots displays the distributions of selected features used to classify signal and peaking background events. The features include the cosine of the angles and the invariant masses involving η, $D^{(*)}$, and ℓ. In signal events, where η and $D^{(*)}$ are direct decay products of D^{**}, the cosine of the angle between η and $D^{(*)}$ (shown in the first row) tends to be close to zero, which reflects their minimal separation angle due to being boosted by the movement of D^{**}. In contrast, in peaking background events, η and $D^{(*)}$ come from different parents, resulting in angles close to 180°. Consequently, the invariant mass of $D^{(*)}\eta$ in signal events aligns closely with the mass of D^{**}, whereas, in the peaking background, these particles are pointing away from each other, which leads to on average higher invariant mass values. On the other hand, between η and ℓ, the reverse pattern is observed: in signal, they are disparate due to different parents, while in the peaking background, a common parent boost aligns them more closely. The numbers above the diagonal in this plot represent the correlation coefficients between features. Consistent with equation 4.10, the cosine of the angle between two particles and their combined invariant mass exhibit anti-correlation.

$$M_{a,b} = \sqrt{M_a^2 + M_b^2 + 2(E_a \cdot E_b - |\vec{p_a}| \cdot |\vec{p_b}| \cdot \cos\alpha_{a,b})} \tag{4.10}$$

where

$$\cos\alpha_{a,b} = \sin\theta_a \cdot \sin\theta_b \cdot (\cos\phi_a \cos\phi_b + \sin\phi_a \sin\phi_b) + \cos\theta_a \cos\theta_b \tag{4.11}$$

The t-SNE (t-distributed Stochastic Neighbor Embedding) plot provides a 2D or 3D map of the original dataset, where each point represents an individual data point. The proximity of points in the plot reflects their similarity: closer points are more similar, while

distant points are less alike [34]. By analyzing the t-SNE plot using the features depicted in Figure 4.18, it is evident that the signal can be quite distinguishable from the peaking background. Despite the relatively low number of peaking background events compared to signal events, the peaking background cluster is localized and not dispersed across the plot. This clustering suggests that even if the number of peaking background events were to increase, they would likely remain concentrated rather than spread out indiscriminately. This concentration supports the effectiveness of the selected features in differentiating between the signal and peaking background.

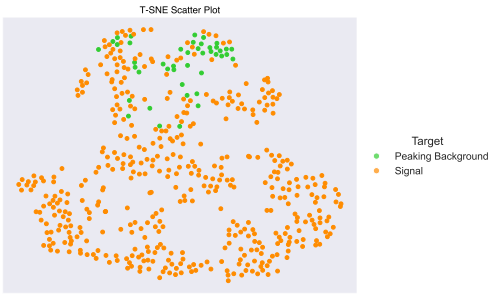

Figure 4.18: **t-SNE Visualization Demonstrating Feature Effectiveness for Signal and Peaking Background Separation** - This t-SNE plot illustrates the effectiveness of the selected features in distinguishing between signal (orange) events and peaking background (green) events. The spatial separation of the two categories within the plot indicates a clear distinction, validating the choice of features for classification. In this plot, the axes do not carry inherent meaning; rather, the crucial information lies in the distance between data points, which reflects the similarity of the data.

Model Training

After selecting the discrimination features, 67% of the dataset was allocated for model training. This portion includes 305 signal events and 27 peaking background events. the chosen model for this analysis is Linear Discriminant Analysis (LDA), which is an extension of Fisher's linear discriminant – a method used for finding a linear combination of features that characterizes or separates two or more classes of objects or events. The model has demonstrated a strong performance with the model accuracy of 90%. The effectiveness of the LDA model in distinguishing between signal and peaking background is shown by the Receiver Operating Characteristic (ROC) [35] curve in Figure 4.19a, which has an Area Under the Curve (AUC) of approximately 0.93. Additionally, the Precision-Recall curve in Figure 4.19b provides further insight, especially valuable in the context of the imbalanced nature of the dataset, with fewer peaking backgrounds than signal events. The Precision-Recall curve

illustrates the balance between precision and recall across varying threshold levels in distinguishing between signal (positive) and peaking background (negative). A substantial area under this curve indicates both high recall and high precision. Here, high precision means a low rate of incorrectly labeling peaking background as a signal (low false positive). In contrast, high recall indicates a low rate of missing actual signal events (low false negatives). Together, these high values demonstrate that the classifier not only accurately identifies signal events (precision) but also successfully captures the majority of these signal instances (recall), effectively differentiating them from the peaking background.

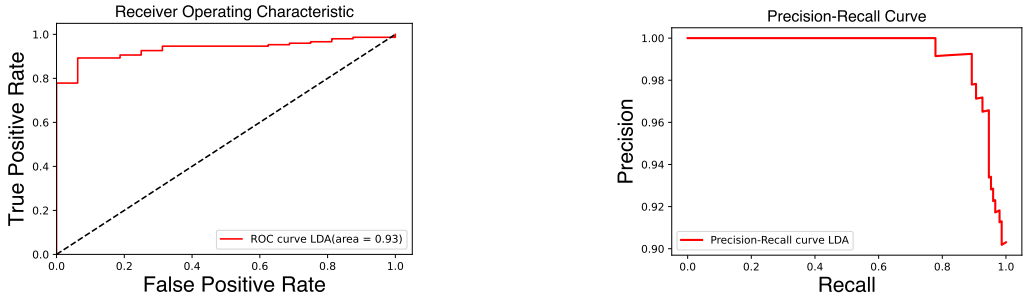

(a) ROC Curve of LDA

(b) Precision-Recall Curve of LDA

Figure 4.19: **Performance Evaluation of LDA Classifier for Signal and Peaking Background Separation** - The displayed plots, (a) Receiver Operating Characteristic (ROC) and (b) Precision-Recall Curve, evaluate the performance of the Linear Discriminant Analysis (LDA) classifier in distinguishing signal from peaking background events. The ROC curve in panel (a) with an area under the curve (AUC) of 0.93, demonstrates the classifier's effectiveness in balancing true positive and false positive rates. Panel (b) illustrates the trade-off between precision, which assesses the accuracy of positive predictions (signal), and recall, which measures the model's ability to identify all positive instances. It highlights the classifier's high precision even at varying levels of recall, which is essential for maintaining reliability in the presence of class imbalance.

The confusion matrix in Figure 4.20 further clarifies the model's effectiveness in classifying signal and peaking background with the chosen threshold of 0.6. With this threshold, the model classifies probabilities greater than or equal to 0.6 as signal candidates and those below as peaking backgrounds. The confusion matrix, representing a snapshot of the model's classification capabilities, reveals a relatively large count of True Positives (TP = 133) and True Negatives (TN = 13), underlying the model's strength in correctly identifying both signal candidates and excluding peaking backgrounds. False Positives (FP = 3) and False Negatives (FN = 16) are relatively low, reflecting the previously discussed precision and recall metrics.

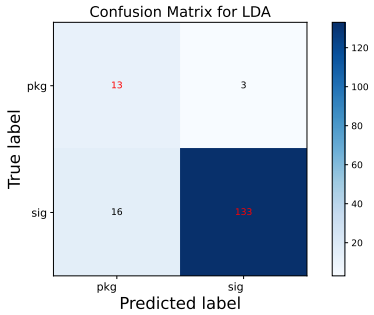

Figure 4.20: **Confusion Matrix for Signal and Peaking Background Classification** - The confusion matrix visualizes the performance of the LDA classifier distinguishing between signal and peaking background events. The metric indicates 133 True Positives (bottom right), where signal candidates are correctly identified; 16 False Negatives (bottom left), where signal candidates are incorrectly labeled as peaking background; and 3 False Positives (top right), where the peaking background is misclassified as signal candidates. Out of 16 events in the testing sample, the model correctly recognized 13 as peaking background (top left).

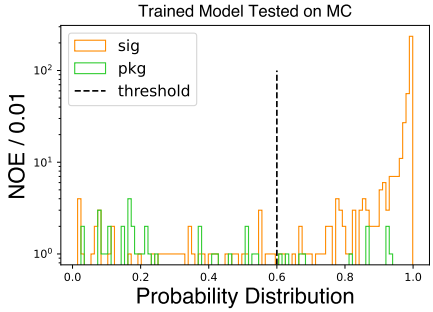

Figure 4.21: **Distribution of Signal and Peaking Background Probabilities with Classification Threshold** - This histogram depicts the distribution of classification probabilities for signal (orange) and peaking background (green) events, with a dashed line indicating the chosen threshold at 0.6. This threshold effectively separates the majority of signal events, which predominantly score above 0.6, from peaking background events, which mostly score below this threshold. The visualization highlights the model's capability to distinguish between signal and background, with a significant proportion of signal correctly identified above the threshold and over 75% of peaking background events accurately classified below it.

Model Results on MC

In evaluating the classifier's performance on the MC dataset, a probability threshold of 0.6, as shown in Figure 4.21, effectively distinguished between signal and peaking background events. Out of 454 signal events, the model correctly identified 410, demonstrating a robust

signal detection capability. Additionally, it correctly classified 33 out of 43 peaking background events, thus accurately recognizing approximately 77% of the peaking background. This result underscores the classifier's effectiveness in discerning between the two categories with considerable precision. Furthermore, the classifier also removed 32% of the combinatorial background after the suppression.

CHAPTER 5

Results

This chapter presents the results derived from the analysis of the signal within the context of double semileptonic B meson decays, and signal efficiency and branching fraction of $B^- \to D^{(*)0}\eta\ell^-\bar{\nu}$ will be discussed. The signal efficiency is calculated using the estimated number of signal candidates obtained from MC simulations and fitting procedures. This efficiency is crucial for determining the branching fraction of the decay $B^- \to D^{(*)0}\eta\ell^-\bar{\nu}$.

5.1 Efficiency

As equation 5.1 illustrates, the efficiency is calculated by dividing the number of signal candidates by the total number of candidates generated in signal mode before any further selections. The number of MC signal candidates is determined by subtracting the number of MC true peaking background events from the estimated number of eta signal events from fit to the MC gamma-gamma mass distribution.

$$\epsilon^{\mathrm{MC}}(\mathrm{signal}) = \frac{N^{\mathrm{MC}}(\mathrm{signal})}{2 \times BF^{\mathrm{MC}}(B^- \to D^{(*)0}\eta\ell^-\bar{\nu}) \times N^{\mathrm{MC}}(B\bar{B}_{\mathrm{charged}})} \tag{5.1}$$

where

$$BF(B^- \to D^{(*)0}\eta l^-\bar{\nu}) = BF(B \to D^{**0}l^-\bar{\nu}) \times BF(D^{**0} \to D^{(*)0}\eta) = 8.04 \times 10^{-3} \tag{5.2}$$

The aim of this analysis is a feasibility study for measuring the branching fraction of $B^- \to D^{(*)0}\eta\ell^-\bar{\nu}$, and the signal sample contains events generated as $B^- \to D^{**0}\ell^-\bar{\nu}$ where D^{**0} decays to $D^{(*)0}\eta$. Thus the entire sample is generated as signal candidates, and therefore the efficiency is calculated by dividing the number of estimated signal candidates (520 ± 61) by the number of generated signal events (4087898) with the integrated luminosity of 470.78 fb^{-1}. The calculated signal efficiency is $(12.71 \pm 1.51) \times 10^{-5}$.

5.2 Branching Fraction

The branching fraction is a measure of the probability or frequency with which a particular decay mode occurs relative to the total number of decays of a particle. As described in equation 5.3, the branching fraction (BF) is calculated by dividing the number of signal events by the products of the signal efficiency and the total number of generated charged generic B mesons. A factor of 2 is included in the denominator to account for the two B mesons in each event, each of which can potentially decay into the signal mode.

$$BF_{(B^- \to D^{(*)0}\eta\ell^-\bar{\nu})} = \frac{N^{\text{pseudo-data}}(\text{signal})}{2 \times \epsilon^{\text{MC}}(\text{signal}) \times N^{\text{pseudo-data}}_{generic}(B\bar{B}_{\text{charged}})} \tag{5.3}$$

The estimated number of eta signal candidates is derived by applying the same function used to describe the eta signal and combinatorial background in MC analysis to pseudo data, as it is shown in Figire 5.1, with parameters fixed as reported in Table 4.2. This yields a total estimated eta signal count of 564 ± 75 events, including both signal and peaking background. From this total, 43 peaking background events are subtracted, resulting in a signal count of 521 ± 75 with the integrated luminosity of 470.78 fb^{-1}. Therefore, the calculated branching fraction is $(8.06 \pm 1.50) \times 10^{-3}$, which is approximately 0.01 standard deviations away from the MC predicted branching fraction of 8.04×10^{-3} for the decay $B^- \to D^{(*)0}\eta\ell^-\bar{\nu}$.

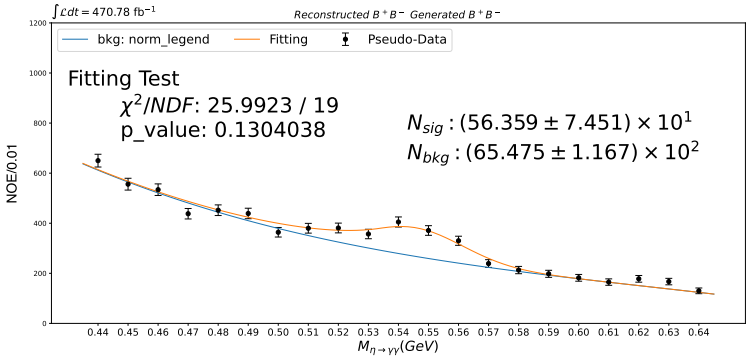

Figure 5.1: **Fit Result of Pseudo-Data for Eta Signal Candidate** - This plot presents the results of fitting the pseudo data to the same function used to fit the MC simulation, with the estimated number of eta signal candidates of 564 ± 75. The fit yields a χ^2 value of 26 with 19 degrees of freedom, resulting in a p-value of 0.13. Since the p-value exceeds 0.05, the fit is considered statistically satisfactory, indicating good agreement between the model and the pseudo-data.

Since the estimated number of eta signal candidates from the fit always includes some peaking background events, the machine learning model described in Section 4.3.2 is applied

to suppress the peaking background and isolate the signal. After this suppression, the calculated branching fraction is $(7.19 \pm 1.41) \times 10^{-3}$, which is found to be consistent with the MC predicted branching fraction of 8.04×10^{-3} for the decay $B^- \to D^{(*)0}\eta\ell^-\bar{\nu}$, differing by only 0.6 standard deviations. The summary of the calculated signal efficiency and the branching fraction for before and after peaking background suppression is presented in Table 5.1.

The same analysis process was applied to another pseudo dataset composed solely of the unrealistic signal modeling in the generic MC sample to cross-check the results. However, the MC sample used for calculating the signal efficiency and, more critically, for training the machine learning model, was a mixture of the signal sample and both peaking and combinatorial backgrounds from the generic sample. As detailed in Section 4.2, the 4-body phase space model in the generic sample does not provide a reliable basis for relying on the kinematics of, for example, the eta meson. Consequently, when the machine learning model – which utilizes kinematic variables to differentiate between signal and peaking background events – is implemented, it fails to accurately classify the signal from peaking background events. This misidentification leads to a significant loss of signal events, classified incorrectly as peaking background. Therefore, the branching fraction calculated using the pure generic sample deviates by more than two standard deviations from the MC branching fraction.

Table 5.1: **Summary of Efficiency and Branching Fraction Before and After Peaking Background Suppression** - The table summarizes the estimated number of eta signal events, signal efficiency, and the branching fraction of the decay mode $B^- \to D^{(*)0}\eta\ell^-\bar{\nu}$ for both scenarios: before and after peaking background suppression. The eta signal counts, which include both signal and peaking background, result from fitting to MC dataset to calculate signal efficiency and to the pseudo dataset for calculating the $B^- \to D^{(*)0}\eta\ell^-\bar{\nu}$. The table also details the number of peaking background events, which decreases by almost 77% following suppression; these peaking background counts are subtracted from the estimated eta signal candidates to compute the signal efficiency. Additionally, the results of the branching fraction using a pure generic sample are included to verify the outcomes from the combined signal and generic samples with the same integrated luminosity 470.78 fb^{-1}

	Before and After Peaking Background Suppression sample: signal + generic $\mathcal{L} = 470.78$ fb^{-1}	
	Before	After
$N^{\mathrm{MC}}(\eta$ signal)	563 ± 61	492 ± 48
N^{MC}(peaking background)	43	10
ϵ^{MC}(signal)	$(12.71 \pm 1.51) \times 10^{-5}$	$(11.80 \pm 1.17) \times 10^{-5}$
$BF^{\mathrm{MC}}_{(B^- \to D^{(*)0}\eta\ell^-\bar{\nu})}$	8.04×10^{-3}	8.04×10^{-3}
$N^{\text{Pseudo-Data}}(\eta$ signal)	564 ± 75	441 ± 73
$BF^{\text{Pseudo-Data}}_{(B^- \to D^{(*)0}\eta\ell^-\bar{\nu})}$	$(8.06 \pm 1.50) \times 10^{-3}$	$(7.19 \pm 1.41) \times 10^{-3}$
	Sanity Check Conducted on Generic Sample sample: generic with $\mathcal{L} = 470.78$ fb^{-1}	
$BF^{\text{Pseudo-Data}}_{(B^- \to D^{(*)0}\eta\ell^-\bar{\nu})}$	$(7.09 \pm 1.57) \times 10^{-3}$	$(4.94 \pm 1.28) \times 10^{-3}$

.

CHAPTER 6

Validations and Cross-checks

6.1 Alternative Fitting Method Employed for Cross-Checking Efficiency

The fitting method used to report the results in Chapter 5 is based on the least squared approach using the `curvefit` package. As previously explained, this method required the addition of flat signal counts when fitting for the crystal ball function parameters. To validate the accuracy of the fitting process, the same procedure of weighting the signal events by different factors was also conducted with an alternative fitting method: the minimum negative log-likelihood approach using the `zfit` package. To cross-check the fitting results, the amount of true MC signal candidates was scaled by a list of different coefficients: [0.25, 0.5, 0.75, 1, 2, 3, 4]. The number of MC peaking background events (43) was added to each of these adjusted signal counts, and the resulting total was then passed to the fitting function. This approach allowed for the analysis of how the fitting function handled varying proportions of signal events – 25%, 50%, 75%, and so on – thereby enabling the calculation of signal efficiency and its associated uncertainty for each scenario. Figure 6.1a illustrates the signal efficiency and its uncertainty for each signal coefficient using both the chi-squared and likelihood fit methods; the results are consistent, with deviations less than one standard deviation between the two fitting approaches. The efficiency is expected to remain approximately flat, considering statistical fluctuations, while the branching fraction is anticipated to change linearly, as depicted in Figure 6.1b. Furthermore, as Figure 6.1a demonstrates, larger uncertainties are observed when the signal candidates are almost negligible compared to the background, and smaller uncertainties occur when the signal candidates constitute a significant portion of the total data.

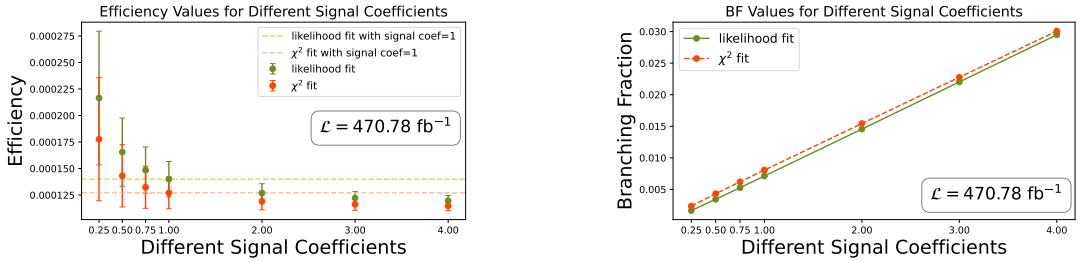

(a) Efficiency Across Signal Coefficients (b) BF Across Signal Coefficients

Figure 6.1: **Comparative Analysis of Efficiency and Branching Fraction Across Different Signal Coefficients Using Likelihood and Chi-Squared Fits** - (a) This graph presents efficiency values for various signal coefficients, comparing outcomes from likelihood and chi-squared fitting methods, with reference lines for both fits at a coefficient of 1. The plot shows larger uncertainties for smaller signal coefficients, with uncertainty reaching about 30%, where the background significantly influences the uncertainty estimation. Conversely, as the signal coefficients increase and the signal candidates become dominant, the effect of the background on uncertainty is significantly reduced, resulting in smaller error bars, approximately 4%. (b) This graph demonstrates the branching fraction results for the same range of signal coefficients, showing a linear increase in estimated branching fraction as the signal coefficient increases, as determined by both fitting techniques.

The uncertainty in the signal efficiency is determined using equation 6.1. N^{MC}(eta signal) represents the number of eta signal candidates estimated from fit, N^{MC}(peaking bkg) refers to the true MC peaking background events, and $N^{\mathrm{MC}}(B\bar{B}_{\mathrm{charged}})$ denotes the total number of generated charged $B\bar{B}$. This involves calculating the uncertainty of N^{MC}(peaking bkg) and $N^{\mathrm{MC}}(B\bar{B}_{\mathrm{charged}})$, $\delta_{N^{\mathrm{MC}}(\text{peaking bkg})}$ and $\delta_{N^{\mathrm{MC}}(B\bar{B}_{\mathrm{charged}})}$ respectively, as the square root of their respective counts, where $\delta_{N^{\mathrm{MC}}(\text{eta signal})}$ is the uncertainty of estimated eta signal candidates obtained from fit. A significant component of the overall uncertainty in the signal efficiency arises from the estimated number of eta signal candidates, where a portion of this uncertainty is attributed to the combinatorial background present within the eta signal region. When only 25% of the signal events are selected (114 events), the estimated number of signal candidates is calculated to be 221 ± 64.

$$\delta_{\epsilon^{\mathrm{MC}}(\text{signal})} = |\epsilon^{\mathrm{MC}}(\text{signal})| \cdot \left[\left(\frac{\delta_{N^{\mathrm{MC}}(\text{eta signal})}}{N^{\mathrm{MC}}(\text{eta signal}) - N^{\mathrm{MC}}(\text{peaking bkg})} \right)^2 + \left(\frac{\delta_{N^{\mathrm{MC}}(\text{peaking bkg})}}{N^{\mathrm{MC}}(\text{eta signal}) - N^{\mathrm{MC}}(\text{peaking bkg})} \right)^2 + \left(\frac{\delta_{N^{\mathrm{MC}}(B\bar{B}_{\text{charged}})}}{N^{\mathrm{MC}}(B\bar{B}_{\text{charged}})} \right)^2 \right]^{\frac{1}{2}} \tag{6.1}$$

Table 6.1: **Estimated Signal Candidates and Uncertainties Across Signal Coefficients** - This table presents the estimated number of signal candidates across a range of signal coefficients using the likelihood fit. Notably, in scenarios where the signal coefficient is below one and the background becomes more dominant, the uncertainty in the estimates remains approximately stable. This observation is consistent with the expectation that the background dominates the uncertainty in the background-dominated region. Comparing the number of signal candidates estimated from the fit with the true number of signal candidates reveals a consistent discrepancy, where the estimated count from the fit is approximately 100 events higher than the true count. This issue will be examined further in detail subsequently.

coef(signal)	0.0	0.25	0.5	0.75	1	2	3	4
$N^{\text{MC-True}}$(signal)	0	114	227	341	454	908	1362	1816
$N^{\text{MC-Fit}}$(signal)	103 ± 63	221 ± 64	338 ± 65	455 ± 67	572 ± 68	1037 ± 73	1498 ± 77	1957 ± 81
Unbiased $N^{\text{MC-Fit}}$(signal)	0 ± 63	118 ± 64	235 ± 65	352 ± 67	469 ± 68	934 ± 73	1395 ± 77	1854 ± 81

As a sanity check, Figure 6.2 presents the ratio of the estimated number of signal candidates, represented in Table 6.1, using the likelihood fit method for various signal coefficients. This is compared once with the number when the coefficient is one, which is 572 events (represented by the blue points), and once with the expected number of signal candidates, which is 454 events (represented by the red points). This comparison not only provides a clear visual assessment of how the fitting process scales with different signal coefficients but also aims to verify if the estimated number of signal candidates changes linearly with the slope of one. This approach validates the consistency of the fit across different signal intensities and checks for proportional scaling in the fitting outputs.

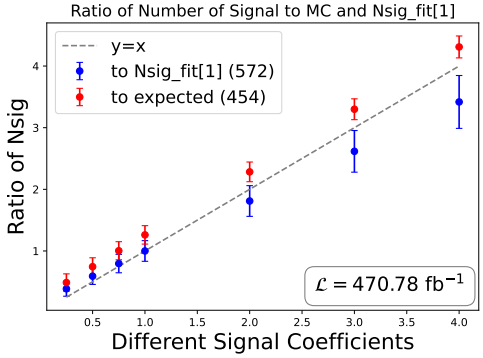

Figure 6.2: **Comparison of Signal Estimation to MC Expectation and Initial Fit Result Across Signal Coefficients** - This plot displays the ratios of the estimated number of signal candidates to the true number of MC signal candidates (454 events), and to the number of obtained from the initial fit at a signal coefficient of 1 (572 events), across varying signal coefficients. The red markers show the ratio to the expected MC value, while the blue markers indicate the ratio to the initial fit result. The dashed line represents a ratio of one, serving as a baseline where the estimates match the referenced value.

A notable observation from Figure 6.2 is that all the red points, which represent the ratio of the estimated number of signal candidates to the expected number of MC signal candidates, consistently appear above the dashed line. This shift could suggest that a certain number of combinatorial background candidates are consistently being counted as part of the eta signal candidates. Furthermore, the error bars on this plot are highly correlated because most of the uncertainty originates from the background, which remains unchanged across different cases despite variations in the number of signal candidates. To investigate this possibility further, another random sample is selected, helping to verify whether the observed shift is an artifact of sample selection or an inherent bias in how the fitting process accounts for the number of eta signal candidates in the eta signal region. Figure 6.3 demonstrates that, across two different random samples, the ratio of the estimated number of signal candidates consistently remains above the slope-one dashed line. This consistent positioning suggests that within the eta signal region, some of the combinatorial background events are being miscounted as eta signal candidates. As demonstrated in Table 6.1 and Figure 6.3, when the signal coefficient is set to 0.0, the model still identifies some signal candidates, amounting to approximately 100 events. A review of all estimated numbers of signal candidates listed in the third row of the table and the corresponding MC true numbers shows a consistent discrepancy of about 100 events. This consistent gap suggests that the number of signal candidates requires calibration. This can be achieved by identifying a trend line from these data points, which shows an intercept of 107 ± 1 events.

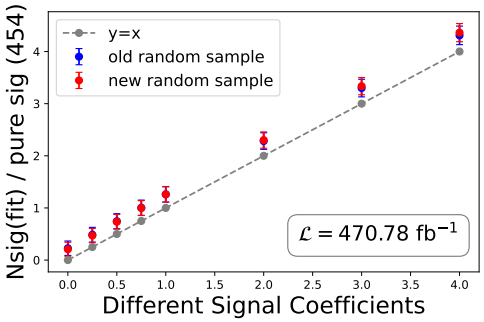

Figure 6.3: **Comparison of Signal Estimates Across Two Random Samples at Various Coefficients** - This plot illustrates the estimated number of signal candidates normalized to the expected MC signal candidates (454 events) for two different random samples, plotted across various signal coefficients. Blue markers denote the old random sample, while red markers represent the new random sample. Each point consistently lies above the dashed reference line y=x, indicating that all estimates exceed the normalized expected value. This consistent overestimation across both samples suggests that some of the combinatorial background within the signal region is being mistakenly counted as an eta signal candidate. Notably, as the signal coefficient increases, the influence of the background decreases; for instance, at a coefficient of 4 the ratio is approximately 5% above the dashed line, whereas of 0.25, where the signal candidates are minimal, the ratio is about 20% above, indicating a stronger background effect at lower signal strengths.

Another aspect investigated was the effect of increasing the signal coefficient to larger values such as 10, 20, and 40. This investigation aimed to observe how the estimated number of signal candidates from the fit responds when the number of MC signal candidates becomes dominant. Figure 6.4 displays the ratio of the estimated number of signal candidates when the signal coefficients are 10, 20, and 40, compared to when the coefficient is 10, to assess whether these ratios scale linearly with a slope of one. If there were significant issues with the fitting process – such as an imbalance in how signal candidates and background are accounted for – it would likely impact the estimation significantly at lower coefficients like one. However, as the coefficient increases to 10, 20, and 40, the signal candidates become so predominant that the influence of the background should diminish markedly. As shown in Figure 6.2, at a coefficient of 4, the relative difference between the estimated signal candidates and the dashed line is about 15%. However, this relative difference gets smaller as the coefficients increase to larger values, such as 40. This trend suggests that the signal candidates itself is consistent and do not have inherent issues. The diminishing relative difference at higher coefficients indicates that any discrepancies observed at lower coefficients are likely due to background effects rather than the signal candidate processing itself.

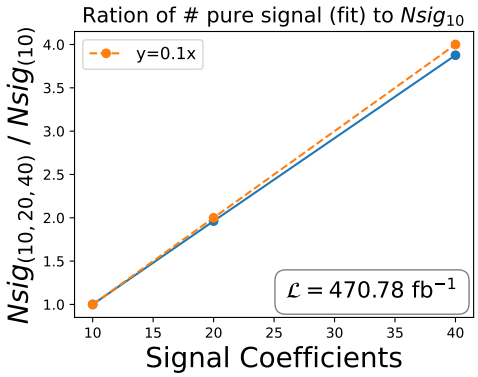

Figure 6.4: **Minimal Impact of Combinatorial Background at High Signal Coefficients** - This graph illustrates the ratio of the number of pure signal events estimated from the fit to the baseline at a signal coefficient of 10 (Nsig10), for coefficients ranging from 10 to 40. The orange dashed line (y=0.1x) indicates an ideal scenario where the estimated signal candidates scale perfectly with increased coefficients. The plot reveals that even as the signal coefficient increases, the deviation from the ideal line remains minimal, less than 5%, demonstrating the linearity of the signal candidates estimate when the background is small.

6.2 Evaluating the Impact of Different Cut Sets on Figure of Merit

To find the optimal sets of ntupe-level cuts, various combinations have been tested. The effectiveness of each set is assessed by calculating the figure of merit (FOM), defined in equation 6.2. In fact, it measures the statistical significance of signal candidates among noise, with a higher FOM indicating a better separation and cleaner signal candidate identification. In Table 6.2, four sets of cuts are defined, each accompanied by its corresponding FOM. The first two rows in the table are based on allowing up to 9 $\Upsilon(4S)$ candidates per event. The first set involves reconstructing the B mesons in the event as charged, yielding an FOM of 6.46. The second set, where one B meson is reconstructed in the signal mode $D^{(*)}\eta\ell\nu$ and the other in the tag mode $D^{(*)}\ell\nu$ shows an improvement with a FOM of 9.10. The third set introduces a further refinement by selecting only one $\Upsilon(4S)$ candidate per event, as detailed in Section 4.2.2; contrary to expectations, this resulted in a 33% decrease in FOM. This drop is because the second set of cuts allowed for multiple $\Upsilon(4S)$ candidates per event (up to 9), The same event can often lead to multiple signal candidates and those events with true signal decays tend to have more signal candidates than background events do. Finally, by selecting the best $\Upsilon(4S)$ candidate and adding an extra cut on the cosine of the angle between B meson and its decay products ($\cos\theta_{\mathrm{BY}}$), which will be discussed in the following

Section (6.2.1), there was an improvement in FOM.

$$\text{FOM} = \frac{N^{\text{MC}}(\text{signal})}{\sqrt{(N^{\text{MC}}(\text{signal}))^2 + (N^{\text{MC}}(\text{combinatorial bkg}))^2}} \tag{6.2}$$

Table 6.2: **Evaluation of Figure of Merit and Efficiency for Various Sets of Cuts** - Below, the Figure Of Merit (FOM) and efficiency for each set of cuts is calculated and displayed. Each subsequent row incorporates all the cuts from the previous row, plus an additional specific cut. Moreover, all four sets include common criteria: no charged particles in the Rest Of Event (ROE) and the energy of the ROE must be below 1 Gev. The first two rows in the table include up to nine $\Upsilon(4S)$ candidates per event.

#	**Cuts** (+ **No Charged Tracks in ROE and Eextra_ROE** < 1)	**FOM**	ϵ^{MC} $\times 10^{-5}$
1	$B^{\pm}$	6.46	69.25
2	$B^- \to D^{(*)0}\eta\ell^-\bar{\nu}$, $B^+ \to \bar{D}^{(*)0}\ell^+\nu$	9.10	34.86
3	$B^- \to D^{(*)0}\eta\ell^-\bar{\nu}$, $B^+ \to \bar{D}^{(*)0}\ell^+\nu$ + Best Candidate	6.09	12.71
4	$B^- \to D^{(*)0}\eta\ell^-\bar{\nu}$, $B^+ \to \bar{D}^{(*)0}\ell^+\nu$ + Best Candidate + $-1.9 < \cos\theta_{\text{BY}} < 1.1$	7.55	12.31

6.2.1 Cosine of the Angle Between B Meson and Its Decay Products ($\cos\theta_{\text{BY}}$)

This variable calculates the cosine of the angle between the momentum vector of the B meson and its visible decay products, denoted as Y, excluding neutrinos. The determination of $\cos\theta_{\text{BY}}$ relies on a mathematical formula that utilizes the momentum vectors of the B meson and its detected decay products, rather than a direct measurement of the angle within the laboratory. Formula 6.3 details how to calculate the $\cos\theta_{\text{BY}}$ variable when $\text{B} \to \text{Y}\nu$.

$$\cos\theta_{\text{BY}} = \frac{2\,\text{E}_\text{B}\text{E}_\text{Y} - \text{M}_\text{B}^2 - \text{M}_\text{Y}^2}{2\,|\vec{\text{p}}_\text{B}||\vec{\text{p}}_\text{Y}|} \tag{6.3}$$

Figure 6.5 illustrates the distribution range for the cosine of the angle between B and Y, which should be between -1 and 1 in an ideal physical scenario and represents the full possible span of angles from 0 to 180 degrees. However, missing particles can lead to mismeasurement of kinematic variables that causes $\cos\theta$ to be more negative ($\cos\theta < -1$). Conversely, the inclusion of additional unrelated particles in the event could produce a $\cos\theta$ value that is more positive ($\cos\theta > +1$).

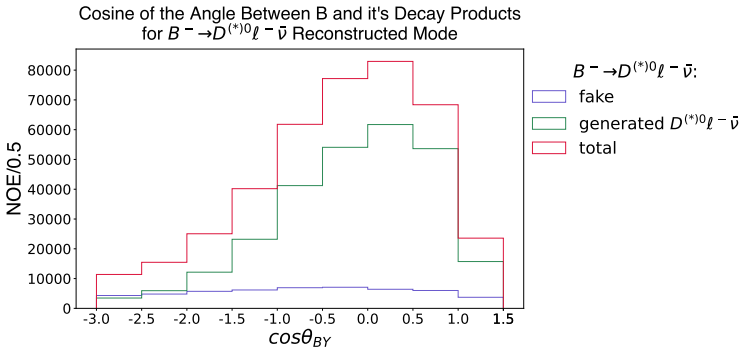

Figure 6.5: **Angular Correlation Distribution for B^- Decay Channels** - This plot illustrates the distribution of a kinematic variable defined as the cosine of the angle ($\cos\theta_{BY}$) between the momentum vectors of the B mesons and their decay products, excluding the neutrino. According to the selection criteria in the BASF2 framework, this variable is constrained to the range between -3 (in case of missing particles) and 1.5 (in case of adding extra particles). The plot displays the range of $\cos\theta_{\mathrm{BY}}$ for the decay mode $B \to D^{(*)}\ell\nu$. It compares the $\cos\theta_{\mathrm{BY}}$ distribution for cases where the B meson was reconstructed within this mode, with scenarios when it was generated as $D^{(*)}\ell\nu$, and with cases where the B mesons originate from alternate decay modes.

CHAPTER 7

Discussion

7.1 Double Semileptonic Decays Advantage

The data selected for this analysis combines a signal sample consisting solely of the generated signal mode and background from a generic sample encompassing all possible B meson modes. Decays in the generic into the $D^{(*)0}\eta\ell^-\bar{\nu}$ have been removed and replaced with the signal sample because the kinematics of the eta meson in the signal mode are reliably represented. Double reconstruction of B mesons, where both the signal B meson (B_{sig}) and the tagging B meson (B_{tag}) are fully reconstructed, is advantageous for several reasons, particularly in enhancing the precision and reducing background noise. By reconstructing both mesons, this method significantly reduces combinatorial background, which arises when particles from different decays are mistakenly combined to mimic a decay signal. Additionally, it minimizes the impact of continuum background, which originates from non-B meson processes, such as the production of lighter quark pairs (e.g., $u\bar{u}$, $d\bar{d}$, $s\bar{s}$, and $c\bar{c}$). The double reconstruction strategy allows for more accurate identification and analysis of the event's kinematics, enabling a clearer separation of signal candidates from the background and improving the overall reliability of measurements, although it will reduce efficiency (Table 6.2).

7.2 Outlook

- In this study, a branching fraction of a decay mode ($B^- \to D^{(*)0}\eta\ell^-\bar{\nu}$) that has never been measured is explored. The sensitivity of measuring this BF using the employed technique can be estimated from the scaled signal studies presented earlier in Chapter 6. As illustrated in the bottom row of Table 6.1, which lists the estimated number of signal candidates across various signal coefficients, the approach allows for an effective projection of the sensitivity per luminosity of the BF measurement.

- The results of this thesis are based on an exploratory study and have not yet been tested

with real data. Therefore, the next step is to apply the developed selection criteria and model to measure the branching fraction of the signal mode $B^- \to D^{(*)0}\eta\ell^-\bar{\nu}$ using actual experimental data.

- Another avenue for further analysis involves applying the same analytical approach to neutral B mesons. As detailed in Section 4.2.5, charged B mesons were primarily selected for this thesis due to their cleaner signal candidates and a larger sample size of reconstructed B mesons. In contrast, only 1709 events of neutral B mesons survived the selection process, constituting about 24% of the charged B mesons sample. Consequently, applying the developed methods to the neutral B mesons sample is anticipated to yield approximately 125 signal events with the signal efficiency of 3×10^{-5}.

- To measure the branching fraction of the signal mode ($B \to D^{(*)}\eta\ell\nu$) in real data, simulations will be used to estimate the number of peaking background candidates and its uncertainty will be determined by varying the branching fractions of the MC decay modes that contribute to it. As indicated in Table 6.1, if the real signal count is zero, a significant $\gamma\gamma$ mass peak is not expected because there would be an estimated 43 peaking backgrounds with an uncertainty of around 60, primarily due to the combinatorial background. Therefore, the peaking background itself falls below the sensitivity threshold of this analysis.

Bibliography

[1] P.A. Zyla et al. (Particle Data Group). "Review of Particle Physics". In: *Prog. Theor. Exp. Phys.* 2020 (Aug. 2020), p. 083C01. ISSN: 2050-3911. eprint: https://academic.oup.com/ptep/article-pdf/2020/8/083C01/34673722/ptaa104.pdf. URL: https://doi.org/10.1093/ptep/ptaa104.

[2] Andreas Höcker and Zoltan Ligeti. "CP Violation and the CKM Matrix". In: *Annual Review of Nuclear and Particle Science* 56.1 (Nov. 2006), pp. 501–567. ISSN: 1545-4134. URL: http://dx.doi.org/10.1146/annurev.nucl.56.080805.140456.

[3] Marina Artuso, Elisabetta Barberio, and Sheldon Stone. "B meson decays". In: *PMC Physics A* 3.1 (Feb. 2009). ISSN: 1754-0410. URL: http://dx.doi.org/10.1186/1754-0410-3-3.

[4] J. Kahn. "The Belle II Experiment". In: *CERN-BINP Workshop for Young Scientists in e+e- Colliders*. 2017, pp. 45–54. DOI: 10.23727/CERN-Proceedings-2017-001.45.

[5] T. Abe et al. *Belle II Technical Design Report*. 2010. arXiv: 1011.0352 [physics.ins-det].

[6] Kou et al. "The Belle II Physics Book". In: *Progress of Theoretical and Experimental Physics* 2019.12 (Dec. 2019). ISSN: 2050-3911. URL: http://dx.doi.org/10.1093/ptep/ptz106.

[7] Izaak Neutelings. *Standard Model (SM) of Particles Physics table*. 2023. URL: https://tikz.net/sm_particles/.

[8] Ziro Maki, Masami Nakagawa, and Shoichi Sakata. "Remarks on the Unified Model of Elementary Particles". In: *Progress of Theoretical Physics* 28.5 (Nov. 1962), pp. 870–880. ISSN: 0033-068X. eprint: https://academic.oup.com/ptp/article-pdf/28/5/870/5258750/28-5-870.pdf. URL: https://doi.org/10.1143/PTP.28.870.

[9] J. H. Christenson et al. "Evidence for the 2π Decay of the K_2^0 Meson". In: *Phys. Rev. Lett.* 13 (4 July 1964), pp. 138–140. URL: https://link.aps.org/doi/10.1103/PhysRevLett.13.138.

[10] David J Griffiths. *Introduction to elementary particles; 2nd rev. version*. Physics textbook. New York, NY: Wiley, 2008. URL: https://cds.cern.ch/record/111880.

[11] Makoto Kobayashi and Toshihide Maskawa. "CP Violation in the Renormalizable Theory of Weak Interaction". In: *Prog. Theor. Phys.* 49 (1973), pp. 652–657. DOI: 10.1143/PTP.49.652.

[12] Z. Ligeti (LBNL) A. Ceccucci (CERN) and Y. Sakai (KEK). *CKM Quark-Mixing Matrix*. Accessed: 2024-03-12. 2022. URL: https://pdg.lbl.gov/2023/reviews/rpp2022-rev-ckm-matrix.pdf.

[13] Ian J.R. Aitchison and Anthony J.G. Hey. *GAUGE THEORIE IN PARTICLE PHYSICS, A PRACTICAL INTRODUCTION, VOLUME 2, Non-Abelian Gauge Theories, QCD and The Electroweak Theory*. URL: https://inspirehep.net/files/460785b7e1e5ef87b7f8d4f9307bd027.

[14] A. J. Bevan. "The Physics of the B Factories". In: *The European Physical Journal C* 74.11 (Nov. 2014). ISSN: 1434-6052. URL: http://dx.doi.org/10.1140/epjc/s10052-014-3026-9.

[15] K. Abe et al. "Observation of Large CP Violation in the Neutral B Meson System". In: *Physical Review Letters* 87.9 (Aug. 2001). ISSN: 1079-7114. URL: http://dx.doi.org/10.1103/PhysRevLett.87.091802.

[16] B. Aubert et al. "Observation of CP Violation in the B0 Meson System". In: *Physical Review Letters* 87.9 (Aug. 2001). ISSN: 1079-7114. URL: http://dx.doi.org/10.1103/PhysRevLett.87.091801.

[17] R. L. Workman et al. "Review of Particle Physics". In: *PTEP* 2022 (2022), p. 083C01. DOI: 10.1093/ptep/ptac097.

[18] Vera G. L¨ uth. *Semileptonic B Meson Decays*. URL: https://www.annualreviews.org/doi/pdf/10.1146/annurev.nucl.012809.104421.

[19] Florian U. Bernlochner et al. "Constraints on exclusive branching fractions $\mathcal{B}_i(B^+ \to X_c^i l^+ \nu)$ from moment measurements in inclusive $B \to X_c l \nu$ decays". In: *Eur. Phys. J. C* 74.6 (2014), p. 2914. DOI: 10.1140/epjc/s10052-014-2914-3. arXiv: 1402.2849 [hep-ph].

[20] Kazunori Akai, Kazuro Furukawa, and Haruyo Koiso. "SuperKEKB Collider". In: *Nucl. Instrum. Meth. A* 907 (2018), pp. 188–199. DOI: 10.1016/j.nima.2018.08.017. arXiv: 1809.01958 [physics.acc-ph].

[21] Belle II Collaboration. *Mass Distribution of Upsilon Resonances*. URL: https://software.belle2.org/development/sphinx/online_book/fundamentals/02-datataking.html.

[22] Y. Makida et al. "Development of a superconducting solenoid magnet system for the B factory detector (BELLE)". In: *Adv. Cryog. Eng.* 43 (1998). Ed. by P. Kittel, pp. 221–228. DOI: 10.1007/978-1-4757-9047-4_25.

[23] Belle II Collaboration. URL: https://www.belle2.org/e21595/.

[24] S Lee et al. "Development of High Level Trigger Software for Belle II at SuperKEKB". In: *Journal of Physics: Conference Series* 331.2 (Dec. 2011), p. 022015. URL: https://dx.doi.org/10.1088/1742-6596/331/2/022015.

[25] Yoshihito Iwasaki et al. "Level 1 trigger system for the Belle II experiment". In: *IEEE Trans. Nucl. Sci.* 58 (2011). Ed. by Sascha Marc Schmeling, pp. 1807–1815. DOI: 10.1109/TNS.2011.2119329.

[26] H. Baer and X. Tata. *Weak scale supersymmetry: From superfields to scattering events*. Cambridge University Press, May 2006. ISBN: 978-0-521-29031-9, 978-0-511-19011-7, 978-0-521-29031-9, 978-0-521-85786-4.

[27] Anders Ryd et al. "EvtGen: A Monte Carlo Generator for B-Physics". In: (May 2005). URL: https://inspirehep.net/literature/707695.

[28] S. Agostinelli et al. "GEANT4–a simulation toolkit". In: *Nucl. Instrum. Meth. A* 506 (2003), pp. 250–303. DOI: 10.1016/S0168-9002(03)01368-8.

[29] John Erthal Gaiser. "Charmonium Spectroscopy From Radiative Decays of the J/ψ and ψ'". Other thesis. Aug. 1982. URL: https://inspirehep.net/files/3a6ffc353519cd9cbac9b439b523ef6d.

[30] J.-F. Krohn et al. "Global decay chain vertex fitting at Belle II". In: *Nuclear Instruments and Methods in Physics Research Section A: Accelerators, Spectrometers, Detectors and Associated Equipment* 976 (2020), p. 164269. ISSN: 0168-9002. URL: https://www.sciencedirect.com/science/article/pii/S0168900220306653.

[31] *Reconstructed Invariant Mass Distribution of Photon Pairs*. URL: https://cerncourier.com/a/lhcf-makes-the-most-of-a-special-run/.

[32] Florian U. Bernlochner and Zoltan Ligeti. "Semileptonic $B_{(s)}$ decays to excited charmed mesons with e, μ, τ and searching for new physics with $R(D^{**})$". In: *Physical Review D* 95.1 (Jan. 2017). ISSN: 2470-0029. URL: https://arxiv.org/abs/1606.09300.

[33] *Total Recorded Integrated Luminosity Up To Now*. URL: https://www.belle2.org/research/luminosity/.

[34] Geoffrey E Hinton and Sam Roweis. "Stochastic Neighbor Embedding". In: *Advances in Neural Information Processing Systems*. Ed. by S. Becker, S. Thrun, and K. Obermayer. Vol. 15. MIT Press, 2002. URL: https://proceedings.neurips.cc/paper_files/paper/2002/file/6150ccc6069bea6b5716254057a194ef-Paper.pdf.

[35] Jesse Davis and Mark Goadrich. "The relationship between Precision-Recall and ROC curves". eng. In: *ACM International Conference Proceeding Series; Vol. 148: Proceedings of the 23rd international conference on Machine learning; 25-29 June 2006*. New York, NY, USA: ACM, 2006, pp. 233–240. ISBN: 9781595933836.